 CMES, vol.84, no.1, pp.41-97, 2012

High-Performance 3D Hybrid/Mixed, and Simple 3D Voronoi Cell Finite Elements, for Macro- & Micro-mechanical Modeling of Solids, Without Using Multi-field Variational Principles

P. L. Bishay[1] **and S.N. Atluri**[1]

Abstract: Higher-order two-dimensional as well as low and higher-order three-dimensional new Hybrid/Mixed (H/M) finite elements based on independently assumed displacement, and judiciously chosen strain fields, denoted by HMFEM-2, are developed here for applications in macro-mechanics. The idea of these new H/M finite elements is based on collocating the components of the independent strain field, with those derived from the independently assumed displacement fields at judiciously and cleverly chosen collocation points inside the element. This is unlike the other techniques used in older H/M finite elements where a two-field variational principle was used in order to enforce both equilibrium and compatibility conditions in a variational sense. The eight- and nine-node quadrilateral iso-parametric elements are used as examples of higher order two-dimensional elements; the eight-node brick element is used as an example of a low order three-dimensional element, while the twenty-node brick element is used as an example of higher order three-dimensional element. The performance of these new elements are compared with those of the primal (displacement-based) finite elements in terms of stability, efficiency, invariance, locking, and sensitivity to mesh distortion in various numerical experiments. All these new H/M elements proved to be stable, invariant, less sensitive to mesh distortion and experience no locking. The superiority of these new HMFEM-2 elements over the displacement-based elements is very much more significant for the low order elements than that for the higher order ones. The performance and efficiency of these new H/M finite elements are much better than that of many other H/M elements in the literature [Pian and co-workers (1964-1984), and Atluri and co-workers (1975-1984)].

The same idea of the simple collocation is used in developing a general three-dimensional Voronoi cell finite element, denoted as VCFEM-RBF-W, based on radial basis functions (RBF) as the interior displacement fields and the Wachspress

[1] Center for Aerospace Research & Education, University of California, Irvine, CA, USA.

Barycentric linear functions as the boundary surface displacement field, for modeling micro-mechanics of solids. The compatibility between the interior and boundary displacements in the present VCFEM-RBF-W element is enforced using two methods: the first by collocation at some carefully chosen points at the boundaries of the VCFEM-RBF-W element, and the second by using the least squares method which can be considered as the limiting case of the collocation method when the number of collocation points increases to infinity. The developed 3D Voronoi cell finite element has an arbitrary number of faces, and each face has an arbitrary number of sides or edges. Some numerical experiments are presented to evaluate the performance of this new element. The VCFEM-RBF-W element is then used in a micro-mechanical application of determining the effective material properties of functionally graded materials (FGM), and the results are found to be in agreement with those of the experiments, and are better than those determined by other models used in the literature. The new VCFEM-RBF-W element formulation is much simpler and efficient, as compared to the VCFEM-HS developed by Ghosh and coworkers (1991-2011), based on Pian's hybrid stress method. The new elements are suitable for extension to dynamical, geometrically nonlinear, elastic-plastic, and fracture analyses.

Keywords: Hybrid/Mixed finite elements, higher order, three-dimensional finite elements, Voronoi cells, radial basis functions, Wachspress Barycentric coordinates, functionally graded materials, collocation, least square, efficiency, invariance, locking.

1 Introduction

In contrast to the popular selective-reduced-integration methods, the use of the multi-field finite element methods may be one of the more rational ways to resolve many problems that the primal displacement-based finite elements suffer from, such as locking phenomena, the difficulty to satisfy higher-order inter-element continuity requirements, the sensitivity to mesh distortion, etc. Generally, these multi-field finite elements are called "hybrid/mixed" finite elements, and were developed in various ways throughout the previous forty years. However, these multi-field finite element methods did not enjoy as much acceptability and use, as their primal counterparts, mainly due to the complexity of their formulations, the difficulty or near-impossibility of satisfying the LBB stability conditions a priori, and in no small measure, due to their very high-cost of computation as compared to the primal (displacement-based) elements.

The two-field finite element, based on assuming both the displacement and stress fields, was the first idea that evolved. This first version was introduced by [Pian

(1964)] as an "equilibrated-stress" finite element, based on applying the modified principle of minimum complementary energy, and using an "a-priori equilibrated" assumed stress field in each element, along with an inter-element compatible displacement field along the element boundaries. Modifying the idea by using an "a-posteriori equilibrated" stress field and an inter-element compatible displacement field inside each element, and applying Reissner's variational principle was done by Atluri and his co-workers in several applications [Atluri (1975); Atluri, Tong, and Murakawa (1983); Cai, Paik, and Atluri (2009); Cai, Paik, and Atluri (2009); Cai, Paik, and Atluri (2010b); Zhu, Cai, Paik, and Atluri (2010); Cai, Paik, and Atluri (2010b); Punch and Atluri (1984b); Punch and Atluri (1984a); Rubinstein, Punch, and Atluri (1984)]. The use of an "a-posteriori equilibrated" stress field is more convenient than the "a-priori-equilibrated" one for the geometrical nonlinear and dynamical problems. Again, [Pian and Wu (1983)] developed a hybrid/mixed finite element based on the modified Reissner's principle [Reissner (1950)] and assuming an incompatible displacement field with the assumed stress field.

On the other hand, the two-field finite element based on assuming both the displacement and strain fields in each element was also developed by Atluri and his co-workers in [Cazzani, Garusi, Tralli, and Atluri (2005); Dong and Atluri (2011a, 2011b, 2012)].

Three-field finite elements were also developed by assuming displacement, stress and strain fields using Hu-Washizu principle in [Atluri (1975); Atluri, Tong, and Murakawa (1983); Tang, Chen, and Liu (1984)].

The hybrid/mixed finite elements were able to demonstrate their advantages in applications which vary from 2D to 3D problems, from solid to fluid mechanics problems and, for solid mechanics, from rod and beam to plate and shell types of structures.

[Cai, Paik, and Atluri (2009); Cai, Paik, and Atluri (2010a); Zhu, Cai, Paik, and Atluri (2010)] developed a locking-free hybrid-mixed rod/beam element for large deformation analysis of space frame structures based on Reissner's variational principle. [Lee and Pian (1978); Cai, Paik, and Atluri (2010b)] modeled locking-free plates and shells in large deformation analysis using Reissner's variational principle. [Pian and Mau (1972); Cazzani, Garusi, Tralli, and Atluri (2005)] developed hybrid assumed strain finite elements to analyze laminated composite plates. [Bratianu and Atluri (1983); Ying and Atluri (1983)] developed stable mixed finite elements for Stokes flows.

Babuska and Brezzi [Babuska (1973); Brezzi (1974)] analyzed the existence, uniqueness, stability and convergence of saddle point problems and established the so-called LBB conditions. Inability to satisfy LBB conditions in general would plague

the solvability and stability of hybrid/mixed finite element equations. Atluri and his co-workers in [Punch and Atluri (1984a); Punch and Atluri (1984b); Rubinstein, Punch, and Atluri (1984); Xue, Karlovitz, and Atluri (1985)] used a sophisticated group theory to develop guidelines for selecting least-order stress interpolations, from which stable and invariant finite elements satisfying LBB conditions can be formulated. [Pian and Wu (1983)] also proposed to choose stress interpolations by matching each stress/strain mode to each of the stress/strain modes derived from non-rigid-body displacement modes. These LBB conditions exist only with the cases of multi-field variational principles, where Lagrangian multipliers are involved. The new H/M elements presented here use the primitive field variational principle, and hence Lagrangian multipliers are not involved, and thus avoid the LBB conditions.

The idea of the Voronoi cell finite element was presented by [Ghosh and Mallett (1994)] to model random composites based on discretizing the solution domain using Dirichlet tessellation, that was introduced in 1991 by [Ghosh and Mukhopadhyay (1991)], and developing the corresponding VCFEM polygonal finite elements to solve problems of micro-mechanics. The 3D version of this VCFEM with ellipsoidal heterogeneities was developed by [Ghosh and Moorthy (2004)]. Ghosh and his co-workers [Ghosh (2011)] use a modified principle of complementary energy based on "a priori equilibrated" stress field inside each element (similar to that of [Pian (1964)]), and continuous displacement field along the element boundaries. However, selecting an "a priori equilibrated" stress field is difficult or even impossible for dynamical and geometrically nonlinear problems. Also, Lagrangian multipliers are involved in the two-field variational principle used by Ghosh and his co-workers, and hence the derived elements suffer from LBB conditions, which are impossible to be satisfied a priori.

This paper extends the idea of assuming independently chosen element interior-displacement, and inter-element compatible boundary-displacement fields, but using the primitive variational principle in the end, to the modeling of three dimensional micro-mechanics problems through the Voronoi cell finite elements (VCFEM). The present work is an extension of the 2D formulations in [Dong and Atluri (2011a, b)]. Radial basis functions-(RBF)-based displacement fields are assumed in the interior of the 3D Voronoi cell, and linear displacement fields are assumed on the boundaries of each cell. The boundary displacements in the present Voronoi cell finite element (VCFEM) are inter-element compatible, and are linear in terms of the Wachspress coordinates. Since the displacements are denoted by the RBF in the interior, and the Wachspress functions at the boundary, the present VCFEM (which has an arbitrary number of faces, each with an arbitrary number of edges) are denoted as VCFEM-RBF-W. The compatibility, between the interior RBF and

the boundary Wachspress functions, can be enforced using two methods. The first is done simply by collocating the two displacement fields at some boundary collocation-points, and the second is done using the least square method which is the limit of the collocation method as the number of collocation points increases to infinity. The present 3D VCFEM-RBF-W element is much simpler and more efficient than the VCFEM-HS developed by Ghosh and co-workers (1991-2011) using the hybrid-stress variational principle of Pian (1964-1984) and a-priori equilibrated-stress fields. This is due to the following limitations in the VCFEM-HS elements developed by Ghosh and co-workers (1991-2011) using Pian's hybrid-stress two field variational principle: (1) there are LBB stability conditions which are impossible to be satisfied a priori, and the idea proposed in [Ghosh and Moorthy (2004)] to assure the satisfaction of the LBB conditions is computationally expensive and can affect the invariance of the element and the accuracy of the solution, (2) there are additional matrices (**H** and **G**) which need to be computed through quadrature in each element, (3) **H** needs to be inverted in each element, and the rank of **G** in each element has to be assured a priori, (4) the equilibrated stress field, as derived from the 3-D Maxwell-Morera stress functions is not always complete.

This paper also uses the newly developed VCFEM-RBF-W elements in an important micro-mechanical application of determining the effective elastic properties of functionally graded materials (FGM).

The paper is organized as follows: Section 2, the basic idea of the new hybrid/mixed finite elements (HMFEM-2 family) is introduced. Section 3 discusses the higher order 2D elements of the HMFEM-2 family (8-node and 9-node quadrilateral elements) and the numerical examples that show their performance from several points of view. Section 4 introduces the 3D version of the lower-order HMFEM-2 (8-node brick element), as well as the 3D higher order version (20-node brick element), and some numerical examples that show the performance of the elements and compare them to the primal displacement-based elements and the hybrid-stress elements. The development of the new three-dimensional Voronoi cell finite element (VCFEM-RBF-W), and the numerical examples and applications of this element are introduced in section 5. The final conclusions are presented in section 6.

2 Basic Idea of the new Hybrid/Mixed finite elements, based on independently assumed strain and displacement fields in each element

One of the main goals of this paper is to develop high-performance lower-order elements in 3-D (8-node iso-parametric elements) by improving on the usual compatible 8-node brick primal (displacement-based) element, by assuming an independent strain-field, which completely eliminates locking in each element, in addition to an element displacement field. The compatibility between the independently assumed

displacement field and locking-free strain field is enforced by collocation at a finite number of judiciously chosen points within the elements. Thus, the use of the two-field variational principles and the attendant LBB conditions are totally avoided. We also show that while the new procedures presented in this paper improve the performance of the low-order elements, such as 8-noded bricks in 3D, dramatically, they do not improve the performance of the higher-order elements much. This is due to the effect of the well-known "limitation principle".

The general geometric interpolation relation for the iso-parametric elements is

$$x_i = \sum_n x_i^{(n)} N^{(n)}(\xi^\gamma) \tag{1}$$

While the general compatible displacement interpolation is

$$u_i = \sum_n u_i^{(n)} N^{(n)}(\xi^\gamma) \tag{2}$$

Where x_i are the global Cartesian coordinates, $x_i^{(n)}$ are the nodal Cartesian coordinates, ξ^γ are the local non-dimensional element curvilinear coordinates, u_i are the Cartesian components of displacements, $u_i^{(n)}$ are nodal displacements, denoted by the vector $\mathbf{q}$ and $N^{(n)}(\xi^\gamma)$ are the shape functions which are polynomials, complete to a certain order.

A strain field, in Cartesian components, can be derived from the displacement field in ξ^γ and can be written in terms of the nodal displacement vector $\mathbf{q}$ as:

$$\varepsilon_{ij} = u_{(i,j)} = \frac{1}{2}(u_{i,j} + u_{j,i}) = \varepsilon_{ij}(\xi^\gamma, \mathbf{q}) \tag{3}$$

An independent strain field may be assumed for these elements, in Cartesian coordinates, as:

$$\varepsilon_{ij}^{In} = \varepsilon_{ij}^{In}(\xi^\gamma, \boldsymbol{\alpha}) \tag{4}$$

Where $\varepsilon_{ij}^{In}(\xi^\gamma, \boldsymbol{\alpha})$, are the carefully chosen simple polynomials (the choices for which are physically motivated) complete to a certain order, and $\boldsymbol{\alpha}$ is a vector containing undetermined parameters.

This independent strain field can also be written in terms of the vector of nodal strains $\mathbf{q}_\varepsilon$ instead of the undetermined parameters $\boldsymbol{\alpha}$, as:

$$\varepsilon_{ij}^{In} = \varepsilon_{ij}^{In}(\xi^\gamma, \mathbf{q}_\varepsilon) \tag{5}$$

In Matrix and vector notation, equation (1) can be written as:

$$\mathbf{x} = \mathbf{N}(\xi^{\gamma})\mathbf{X} \tag{6}$$

where $\mathbf{X}$ is the nodal coordinate vector, and equations (2) and (3) can be written as:

$$\mathbf{u} = \mathbf{N}(\xi^{\gamma})\mathbf{q} \tag{7}$$

$$\boldsymbol{\varepsilon} = \mathbf{u}_{(i,j)} = \mathbf{B}(\xi^{\gamma})\mathbf{q} \tag{8}$$

$\boldsymbol{\varepsilon}$ or $\mathbf{u}_{(i,j)}$ are the strains derived from the independently assumed displacement field of equation (7). We can also write equations (4) and (5) as:

$$\boldsymbol{\varepsilon}^{In} = \mathbf{A}(\xi^{\gamma})\boldsymbol{\alpha} = \mathbf{N}_{\varepsilon}(\xi^{\gamma})\mathbf{q}_{\varepsilon} \tag{9}$$

Where $\boldsymbol{\varepsilon}^{In}$ is the independently assumed strain tensor, $\mathbf{N}_{\varepsilon}(\xi^{\gamma})$ are the shape functions for the independent strain field.

Then the Cauchy's stress tensor $\boldsymbol{\sigma}$ and the traction vector $\mathbf{t}$ on a surface whose unit normal vector is $\mathbf{n}$ have the forms:

$$\boldsymbol{\sigma} = \mathbf{D}\boldsymbol{\varepsilon}^{In} \tag{10}$$

$$\mathbf{t} = \mathbf{n}\boldsymbol{\sigma} \tag{11}$$

Where $\mathbf{D}$ is the material stiffness tensor.

The basic idea of HMFEM-2 is to enforce compatibility of the independently assumed strains, and the strains derived from the independently assumed displacements, at several pre-selected collocation points $\xi^{\gamma k}$, k = 1, 2, ..., M, leading to:

$$\varepsilon_{ij}^{In}(\xi^{\gamma k}, \boldsymbol{\alpha}) = \varepsilon_{ij}(\xi^{\gamma k}, \mathbf{q}) \quad \text{or alternatively} \quad \varepsilon_{ij}^{In}(\xi^{\gamma k}, \mathbf{q}_{\varepsilon}) = \varepsilon_{ij}(\xi^{\gamma k}, \mathbf{q}) \tag{12}$$

Where $\varepsilon_{ij}^{In}(\xi^{\gamma k}, \boldsymbol{\alpha})$ or $\varepsilon_{ij}^{In}(\xi^{\gamma k}, \mathbf{q}_{\varepsilon})$, and $\varepsilon_{ij}(\xi^{\gamma k}, \mathbf{q})$, are the independently assumed strain field, and the strain field derived from the displacement field, respectively, at point $\xi^{\gamma k}$. It is not necessary to collocate all the strain components at the same points $\xi^{\gamma k}$. Which strain component is collocated at which points in the element, can be based on the judiciously chosen physical behavior of the element.

By judiciously selecting enough collocation equations, we can express the vector $\boldsymbol{\alpha}$ or the nodal strains vector $\mathbf{q}_{\varepsilon}$ in terms of the nodal displacement vector $\mathbf{q}$:

$$\boldsymbol{\alpha} = \mathbf{C}\mathbf{q} \quad \text{or equivalently} \quad \mathbf{q}_{\varepsilon} = \mathbf{E}\mathbf{q} \tag{13}$$

Hence, the strain and stress fields can be expressed in terms of $\mathbf{q}$, as:

$$\boldsymbol{\varepsilon}^{In} = \mathbf{A}(\xi^{\gamma})\mathbf{C}\mathbf{q} = \mathbf{N}_{\varepsilon}(\xi^{\gamma})\mathbf{E}\mathbf{q} = \mathbf{B}^{*}(\xi^{\gamma})\mathbf{q} \tag{14}$$

$$\boldsymbol{\sigma} = \mathbf{D}\boldsymbol{\varepsilon}^{In} = \mathbf{D}\mathbf{A}(\xi^{\gamma})\mathbf{C}\mathbf{q} = \mathbf{D}\mathbf{N}_{\varepsilon}(\xi^{\gamma})\mathbf{E}\mathbf{q} = \mathbf{D}\mathbf{B}^{*}(\xi^{\gamma})\mathbf{q} \tag{15}$$

Now, we can use the principle of minimum potential energy applied to the following primitive-field functional to derive the stiffness matrix of HMFEM-2 family.

$$\pi(u_i) = \sum_{m} \left\{ \int_{\Omega_m} \left[W(\varepsilon_{ij}(u_k)) - \overline{f_i} u_i \right] d\Omega - \int_{S_{tm}} \overline{t_i} u_i dS \right\} \tag{16}$$

Where Ω_m is a subdomain (finite element) from the discretized domain Ω, S_{tm} is the traction boundary of the subdomain Ω_m and is a subset from S_t the traction boundary of the domain Ω, $\overline{f_i}$ and $\overline{t_i}$ are components of prescribed body force, and boundary traction vectors respectively.

$W = W(\varepsilon_{ij}(u_k))$ is the energy density function expressed here is terms of strain field ε_{ij} which, in turn, is expressed in terms of displacement u_k.

For a linear elastic solid, the constitutive equation has the form:

$$\sigma_{ij} = \frac{\partial W}{\partial \varepsilon_{ij}}; \; W = \frac{1}{2} E_{ijkl} \varepsilon_{ij} \varepsilon_{kl} \quad \text{in } \Omega \tag{17}$$

Considering a compatible displacement field which satisfies the constitutive equation (17), the displacement boundary condition:

$$u_i = \overline{u_i} \quad \text{at } S_u, \tag{18}$$

and the displacement compatibility at each inter-subdomain:

$$u_i^{+} = u_i^{-} \quad \text{at } \rho_m \tag{19}$$

a priori, we can use the functional of equation (16) to derive the static equilibrium equation:

$$\sigma_{ij,j} + \overline{f_i} = 0; \quad \sigma_{ij} = \sigma_{ji} \quad \text{in } \Omega, \tag{20}$$

the traction boundary condition:

$$n_j \sigma_{ij} = \overline{t_i} \quad \text{at } S_t, \tag{21}$$

and the traction reciprocity condition at each inter-subdomain boundary:

$$(n_j \sigma_{ij})^{+} + (n_j \sigma_{ij})^{-} = 0 \quad \text{at } \rho_m \tag{22}$$

Where S_u is the displacement boundary of the domain Ω, and ρ_m is the internal subdomain boundary (or the portion of the subdomain boundary that is intersecting with neither S_t the traction boundary, nor S_u the displacement boundary).

The same functional (16) which is used to develop the displacement-based primal finite elements, based on assuming the displacement field only and suffers from the well-known locking phenomena (the normal and the shear strains derived from the displacement field are locked together), can now be used to develop the new HMFEM-2 elements by applying the principle of minimum potential energy as follows:

$$\delta\pi(\mathbf{q}) = \delta\sum_m \left\{ \int_{\Omega_m} \left[\frac{1}{2}\mathbf{q}^T \mathbf{B}^{*T}(\xi^\gamma)\mathbf{D}\mathbf{B}^*(\xi^\gamma)\mathbf{q} - \mathbf{q}^T \mathbf{N}^T(\xi^\gamma)\bar{\mathbf{f}} \right] d\Omega - \int_{S_{tm}} \mathbf{q}^T \mathbf{N}^T(\xi^\gamma)\bar{\mathbf{t}} dS \right\} \tag{23}$$

Setting $\delta\pi(\mathbf{q})$ equals to zero, we get:

$$\sum_m (\mathbf{q}^T \mathbf{K}^e \mathbf{q} - \mathbf{q}^T \mathbf{Q}) = 0, \quad \text{or} \quad \sum_m (\mathbf{K}^e \mathbf{q} - \mathbf{Q}) = 0 \tag{24}$$

Where

$$\mathbf{K}^e = \int_{\Omega_m} \mathbf{B}^{*T}(\xi^\gamma)\mathbf{D}\mathbf{B}^*(\xi^\gamma) d\Omega \tag{25}$$

and

$$\mathbf{Q} = \int_{\Omega_m} \mathbf{N}^T(\xi^\gamma)\bar{\mathbf{f}} d\Omega + \int_{S_{tm}} \mathbf{N}^T(\xi^\gamma)\bar{\mathbf{t}} dS \tag{26}$$

The independently assumed strain field ε_{ij}^{In} is used in the constitutive equation (17) and the functional of equation (16) to derive the stiffness matrix (25).

It is important to note that using the functional of equation (16) as a primitive field functional, using the strains expressed in terms of nodal displacements is not plagued with the so-called LBB conditions because Lagrangian multiplier functions are not involved as in the case of the two-field variational principle (u_i and σ_{ij} or u_i and ε_{ij}).

3 Isoparametric higher order two-dimensional Hybrid/Mixed quadrilateral element

3.1 Eight-node H/M Quadrilateral Element

In order for the element to be invariant (i.e., the element properties, such as the eigenvalues of the stiffness matrix, are not changed according to the orientation

of the global Cartesian coordinate system, or the observer's point of view), an element-fixed set of local orthogonal coordinates is used. Whatever the rotation of the global Cartesian coordinate system $x_1 - x_2 - x_3$, the element-fixed local curvilinear coordinates $\xi^1 - \xi^2$, as well as the element-fixed local orthogonal base vectors $\hat{\mathbf{g}}_\mathbf{1} - \hat{\mathbf{g}}_\mathbf{2}$ will be kept invariant.

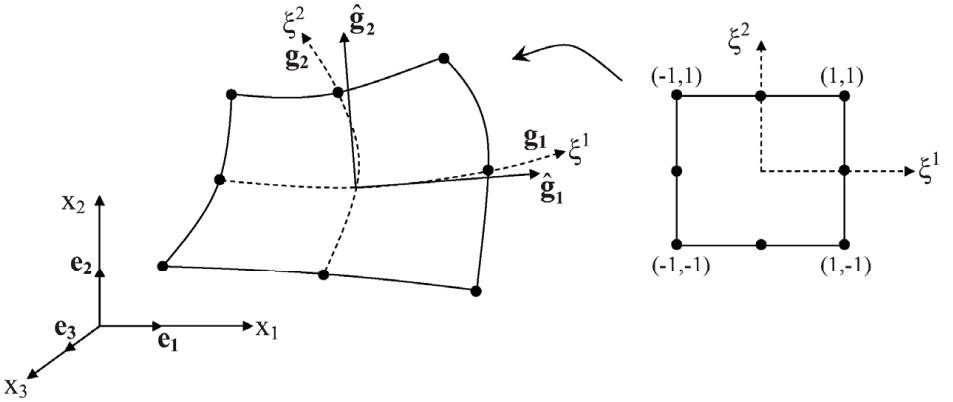

Figure 1: Global Cartesian coordinates, curvilinear coordinates, and element-fixed orthogonal base vectors for the eight-node quadrilateral finite element

Figure 1 shows the eight-node quadrilateral element in global Cartesian coordinates $x_1 - x_2 - x_3$ in the direction of the orthogonal base vectors $\mathbf{e_1} - \mathbf{e_2} - \mathbf{e_3}$, the element-fixed curvilinear coordinates $\xi^1 - \xi^2$, and the covariant base vectors $\mathbf{g_1} - \mathbf{g_2}$ in their directions, and the element-fixed local orthogonal base vectors $\hat{\mathbf{g}}_\mathbf{1} - \hat{\mathbf{g}}_\mathbf{2}$. The isoparametric mapping transforms the regular element in the non-dimensional coordinates $\xi^1 - \xi^2$ that varies from -1 to 1 into the irregular element in the Cartesian $x_1 - x_2$ coordinates.

The element-fixed local orthogonal base vectors $\hat{\mathbf{g}}_\mathbf{1} - \hat{\mathbf{g}}_\mathbf{2}$ are defined as follows: $\hat{\mathbf{g}}_\mathbf{1}$ is in the same direction as that of the covariant base vector $\mathbf{g_1}$ evaluated at the center (0, 0), and $\hat{\mathbf{g}}_\mathbf{2}$ is obtained by rotating $\hat{\mathbf{g}}_\mathbf{1}$ around $\mathbf{e_3}$ counterclockwise by 90^o.

$\mathbf{g_1}$ can be obtained from the following relation:

$$\mathbf{g_1} = \frac{\partial \mathbf{R}}{\partial \xi^1} = \frac{\partial x_1}{\partial \xi^1}\mathbf{e_1} + \frac{\partial x_2}{\partial \xi^1}\mathbf{e_2} \tag{27}$$

Using equation (1), we can write $\mathbf{g_1}$ as:

$$\mathbf{g_1} = \frac{\partial \mathbf{R}}{\partial \xi^1} = \sum_n \left(\frac{\partial N^{(n)}(\xi^1, \xi^2)}{\partial \xi^1} x_1^{(n)} \mathbf{e_1} + \frac{\partial N^{(n)}(\xi^1, \xi^2)}{\partial \xi^1} x_2^{(n)} \mathbf{e_2} \right) \tag{28}$$

Then, $\hat{\mathbf{g}}_{\mathbf{1}}$ and $\hat{\mathbf{g}}_2$ have the forms:

$$\hat{\mathbf{g}}_{\mathbf{1}} = \mathbf{g}_{\mathbf{1}}(0,0) = \sum_n \left(\frac{\partial N^{(n)}}{\partial \xi^1}(0,0) x_1^{(n)} \mathbf{e_1} + \frac{\partial N^{(n)}}{\partial \xi^1}(0,0) x_2^{(n)} \mathbf{e_2} \right) \tag{29}$$

$$\hat{\mathbf{g}}_2 = \mathbf{e}_3 \times \hat{\mathbf{g}}_1 = \sum_n \left(-\frac{\partial N^{(n)}}{\partial \xi^1}(0,0) x_2^{(n)} \mathbf{e_1} + \frac{\partial N^{(n)}}{\partial \xi^1}(0,0) x_1^{(n)} \mathbf{e_2} \right) \tag{30}$$

Because we are using covariant base vectors, the contravariant components of the independent strain field are specified in terms of the element-fixed non-dimensional coordinates and undetermined coefficients as follows:

$$\begin{aligned} \hat{\varepsilon}^{In11} = {} & \alpha_1 + \alpha_2 \xi^1 + \alpha_3 \xi^2 + \alpha_4 \xi^1 \xi^2 + \alpha_5 (\xi^1)^2 + \alpha_6 (\xi^2)^2 + \alpha_7 (\xi^1)^2 \xi^2 \\ & + \alpha_8 (\xi^2)^2 \xi^1 + \alpha_9 (\xi^1)^2 (\xi^2)^2 \end{aligned} \tag{31}$$

This can be written as in equation (9):

$$\hat{\varepsilon}^{In11} = \mathbf{A_N}(\xi^\gamma) \boldsymbol{\alpha} \tag{32}$$

Where:

$$\mathbf{A_N}(\xi^\gamma) = \begin{bmatrix} 1 & \xi^1 & \xi^2 & \xi^1\xi^2 & (\xi^1)^2 & (\xi^2)^2 & (\xi^1)^2\xi^2 & (\xi^2)^2\xi^1 & (\xi^1)^2(\xi^2)^2 \end{bmatrix}$$

and $\boldsymbol{\alpha} = \begin{bmatrix} \alpha_1 & \alpha_2 & \alpha_3 & \alpha_4 & \alpha_5 & \alpha_6 & \alpha_7 & \alpha_8 & \alpha_9 \end{bmatrix}^T$.
Similarly, we can write:

$$\hat{\varepsilon}^{In22} = \mathbf{A_N}(\xi^\gamma) \boldsymbol{\beta}; \quad \boldsymbol{\beta} = \begin{bmatrix} \beta_1 & \beta_2 & \ldots & \beta_9 \end{bmatrix}^T \tag{33}$$

$$\hat{\varepsilon}^{In12} = \mathbf{A_s}(\xi^\gamma) \boldsymbol{\gamma}; \quad \boldsymbol{\gamma} = \begin{bmatrix} \gamma_1 & \ldots & \gamma_4 \end{bmatrix}^T \tag{34}$$

Where

$$\mathbf{A_s}(\xi^\gamma) = \begin{bmatrix} 1 & \xi^1 & \xi^2 & \xi^1\xi^2 \end{bmatrix}$$

$\boldsymbol{\alpha}, \boldsymbol{\beta}$, and $\boldsymbol{\gamma}$ are vectors of undetermined parameters. Note that the independently assumed element shear strain is of a low-order, and does not involve any parasitic coupling with the normal strains. Also note that the present element has 16 nodal displacement degrees of freedom, and 13 non-rigid-body modes. However the independently assumed strain field has 22 undetermined parameters. This will be seen later, to lead to the effect of the "limitation principle"

The transformation of the strain components from the element-fixed local orthogonal coordinates to the global Cartesian coordinates follows this relation;

$$\varepsilon_{ij} = \hat{\varepsilon}^{kl}(\hat{\mathbf{g}}_\mathbf{k}.\mathbf{e}_\mathbf{i})(\hat{\mathbf{g}}_\mathbf{l}.\mathbf{e}_\mathbf{j}) \tag{35}$$

i.e.

$$\begin{aligned}
\varepsilon_{11} &= \hat{\varepsilon}^{11}(\hat{\mathbf{g}}_1.\mathbf{e}_1)(\hat{\mathbf{g}}_1.\mathbf{e}_1) + \hat{\varepsilon}^{22}(\hat{\mathbf{g}}_2.\mathbf{e}_1)(\hat{\mathbf{g}}_2.\mathbf{e}_1) + \hat{\varepsilon}^{12}(\hat{\mathbf{g}}_1.\mathbf{e}_1)(\hat{\mathbf{g}}_2.\mathbf{e}_1) + \hat{\varepsilon}^{21}(\hat{\mathbf{g}}_2.\mathbf{e}_1)(\hat{\mathbf{g}}_1.\mathbf{e}_1) \\
\varepsilon_{22} &= \hat{\varepsilon}^{11}(\hat{\mathbf{g}}_1.\mathbf{e}_2)(\hat{\mathbf{g}}_1.\mathbf{e}_2) + \hat{\varepsilon}^{22}(\hat{\mathbf{g}}_2.\mathbf{e}_2)(\hat{\mathbf{g}}_2.\mathbf{e}_2) + \hat{\varepsilon}^{12}(\hat{\mathbf{g}}_1.\mathbf{e}_2)(\hat{\mathbf{g}}_2.\mathbf{e}_2) + \hat{\varepsilon}^{21}(\hat{\mathbf{g}}_2.\mathbf{e}_2)(\hat{\mathbf{g}}_1.\mathbf{e}_2) \\
\varepsilon_{12} &= \hat{\varepsilon}^{11}(\hat{\mathbf{g}}_1.\mathbf{e}_1)(\hat{\mathbf{g}}_1.\mathbf{e}_2) + \hat{\varepsilon}^{22}(\hat{\mathbf{g}}_2.\mathbf{e}_1)(\hat{\mathbf{g}}_2.\mathbf{e}_2) + \hat{\varepsilon}^{12}(\hat{\mathbf{g}}_1.\mathbf{e}_1)(\hat{\mathbf{g}}_2.\mathbf{e}_2) + \hat{\varepsilon}^{21}(\hat{\mathbf{g}}_2.\mathbf{e}_1)(\hat{\mathbf{g}}_1.\mathbf{e}_2) \\
\varepsilon_{21} &= \hat{\varepsilon}^{11}(\hat{\mathbf{g}}_1.\mathbf{e}_2)(\hat{\mathbf{g}}_1.\mathbf{e}_1) + \hat{\varepsilon}^{22}(\hat{\mathbf{g}}_2.\mathbf{e}_2)(\hat{\mathbf{g}}_2.\mathbf{e}_1) + \hat{\varepsilon}^{12}(\hat{\mathbf{g}}_1.\mathbf{e}_2)(\hat{\mathbf{g}}_2.\mathbf{e}_1) + \hat{\varepsilon}^{21}(\hat{\mathbf{g}}_2.\mathbf{e}_2)(\hat{\mathbf{g}}_1.\mathbf{e}_1)
\end{aligned} \tag{36}$$

Using the fact that $\varepsilon_{ij} = \varepsilon_{ji}$ and $\hat{\varepsilon}^{kl} = \hat{\varepsilon}^{lk}$, equation (36) can be written as:

$$\begin{Bmatrix} \varepsilon_{11} \\ \varepsilon_{22} \\ 2\varepsilon_{12} \end{Bmatrix} =$$

$$\begin{bmatrix} (\hat{\mathbf{g}}_1.\mathbf{e}_1)^2 & (\hat{\mathbf{g}}_2.\mathbf{e}_1)^2 & (\hat{\mathbf{g}}_1.\mathbf{e}_1)(\hat{\mathbf{g}}_2.\mathbf{e}_1) \\ (\hat{\mathbf{g}}_1.\mathbf{e}_2)^2 & (\hat{\mathbf{g}}_2.\mathbf{e}_2)^2 & (\hat{\mathbf{g}}_1.\mathbf{e}_2)(\hat{\mathbf{g}}_2.\mathbf{e}_2) \\ 2(\hat{\mathbf{g}}_1.\mathbf{e}_1)(\hat{\mathbf{g}}_1.\mathbf{e}_2) & 2(\hat{\mathbf{g}}_2.\mathbf{e}_1)(\hat{\mathbf{g}}_2.\mathbf{e}_2) & (\hat{\mathbf{g}}_1.\mathbf{e}_1)(\hat{\mathbf{g}}_2.\mathbf{e}_2) + (\hat{\mathbf{g}}_2.\mathbf{e}_1)(\hat{\mathbf{g}}_1.\mathbf{e}_2) \end{bmatrix} \begin{Bmatrix} \hat{\varepsilon}^{11} \\ \hat{\varepsilon}^{22} \\ 2\hat{\varepsilon}^{12} \end{Bmatrix} \tag{37}$$

or, $\boldsymbol{\varepsilon} = \mathbf{T}\hat{\boldsymbol{\varepsilon}}$

Where $\mathbf{T}$ is a transformation matrix.

Because the collocation of the strain fields should be done in the local orthogonal coordinate system, we should first transform the components of the strain tensor, derived from the displacement field, from the Cartesian coordinate system to this local orthogonal coordinate system according to equation (37).

$$\hat{\boldsymbol{\varepsilon}} = \mathbf{T}^{-1}\boldsymbol{\varepsilon} = \mathbf{T}^{-1}\mathbf{B}(\xi^\gamma)\mathbf{q} = \hat{\mathbf{B}}(\xi^\gamma)\mathbf{q} \tag{38}$$

[Dong and Atluri (2011a)] proved that in order for the HMFEM-2 elements to pass the patch test, the collocation of strain fields should be done at Gauss quadrature points.

Here, collocation is done by equating the two direct (or normal) strain fields at the 9 points of the 3×3 Gauss quadrature points (points 9-17 in Figure 2 (left)), while

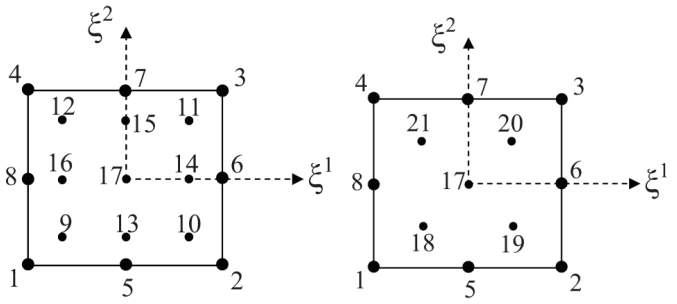

Figure 2: The eight-node quadrilateral element in the non-dimensional coordinate system with the 3×3 (left) and 2×2 (right) Gauss quadrature points

the shear strains are collocated at the 4 points of the 2×2 Gauss quadrature points (points 18-21 in Figure 2 (right)).

So for the normal strains in the 1 direction, we have:

$$\hat{\varepsilon}^{In11}(\xi^{\gamma k}) = \hat{\varepsilon}^{11}(\xi^{\gamma k}) \quad \text{where } \xi^{\gamma k} \text{ are the coordinates of points } 9-17 \tag{39}$$

This produces nine equations in the nine undetermined parameters, thus we can write in matrix notation:

$$\mathbf{G}\boldsymbol{\alpha} = \hat{\boldsymbol{\varepsilon}}^{11} = \hat{\mathbf{B}}_{\mathbf{1}}.\mathbf{q}$$

Where $\mathbf{G}$ is a constant matrix whose rows are the substitution of the coordinates of the collocation points in the matrix $\mathbf{A_N}(\xi^{\gamma})$, and $\hat{\mathbf{B}}_{\mathbf{1}}$ is a constant matrix whose rows are the substitution of the coordinates of the collocation points in the first row of the $\hat{\mathbf{B}}$ matrix (corresponding to the normal strain in the 1-1 direction) of the strain field derived from the displacement field. Thus,

$$\boldsymbol{\alpha} = \mathbf{G}^{-1}\hat{\boldsymbol{\varepsilon}}^{11} = \mathbf{G}^{-1}\hat{\mathbf{B}}_{\mathbf{1}}.\mathbf{q} \tag{40}$$

Similarly, we can get:

$$\boldsymbol{\beta} = \mathbf{G}^{-1}\hat{\boldsymbol{\varepsilon}}^{22} = \mathbf{G}^{-1}\hat{\mathbf{B}}_{\mathbf{2}}.\mathbf{q} \tag{41}$$

$$\boldsymbol{\gamma} = \mathbf{G}_{\mathbf{s}}^{-1}\hat{\boldsymbol{\varepsilon}}^{12} = \mathbf{G}_{\mathbf{s}}^{-1}\hat{\mathbf{B}}_{\mathbf{s}}.\mathbf{q} \tag{42}$$

Thus, the independent strain field can be written now in terms of the nodal displacements as:

$$\hat{\varepsilon}^{In11} = \mathbf{A_N}(\xi^{\gamma})\boldsymbol{\alpha} = \boldsymbol{A}_{\mathbf{N}}(\xi^{\gamma})\mathbf{G}^{-1}\hat{\mathbf{B}}_{\mathbf{1}}.\mathbf{q}$$
$$\hat{\varepsilon}^{In22} = \mathbf{A_N}(\xi^{\gamma})\boldsymbol{\beta} = \mathbf{A_N}(\xi^{\gamma})\mathbf{G}^{-1}\hat{\mathbf{B}}_{\mathbf{2}}.\mathbf{q}$$
$$\hat{\varepsilon}^{In12} = \mathbf{A_s}(\xi^{\gamma})\boldsymbol{\gamma} = \mathbf{A_s}(\xi^{\gamma})\mathbf{G}_{\mathbf{s}}^{-1}\hat{\mathbf{B}}_{\mathbf{s}}.\mathbf{q}$$

This can be combined as:

$$\hat{\boldsymbol{\varepsilon}}^{In} = \begin{bmatrix} \mathbf{A_N}(\xi^\gamma) & \mathbf{0} & \mathbf{0} \\ \mathbf{0} & \mathbf{A_N}(\xi^\gamma) & \mathbf{0} \\ \mathbf{0} & \mathbf{0} & \mathbf{A_s}(\xi^\gamma) \end{bmatrix} \begin{Bmatrix} \mathbf{G}^{-1}\hat{\mathbf{B}}_\mathbf{1} \\ \mathbf{G}^{-1}\hat{\mathbf{B}}_\mathbf{2} \\ \mathbf{G_s}^{-1}\hat{\mathbf{B}}_\mathbf{s} \end{Bmatrix} = \mathbf{A}(\xi^\gamma)\mathbf{C}\mathbf{q} = \hat{\mathbf{B}}^*\mathbf{q} \tag{43}$$

Where,

$$\mathbf{A}(\xi^\gamma) = \begin{bmatrix} \mathbf{A_N}(\xi^\gamma) & \mathbf{0} & \mathbf{0} \\ \mathbf{0} & \mathbf{A_N}(\xi^\gamma) & \mathbf{0} \\ \mathbf{0} & \mathbf{0} & \mathbf{A_s}(\xi^\gamma) \end{bmatrix}, \ \mathbf{C} = \begin{Bmatrix} \mathbf{G}^{-1}\hat{\mathbf{B}}_\mathbf{1} \\ \mathbf{G}^{-1}\hat{\mathbf{B}}_\mathbf{2} \\ \mathbf{G_s}^{-1}\hat{\mathbf{B}}_\mathbf{s} \end{Bmatrix} \text{ and } \hat{\mathbf{B}}^* = \mathbf{A}(\xi^\gamma)\mathbf{C} \tag{44}$$

It should be clearly noted that, in equation (43), one needs to invert the (9×9) matrix $\mathbf{G}$, and a (4×4) matrix $\mathbf{G_s}$. However, no element integrations are necessary, to evaluate these matrices, $\mathbf{G}$ and $\mathbf{G_s}$. In contrast, if a two-field variatioal principle were to have been used, there would have been a need to use element-integration to evaluate a (22×22) element-matrix $\mathbf{H}$ which needs to be inverted for each element, and a (22×16) matrix $\mathbf{G}$ (whose minimum rank must be 13).

Now, after determining the independent strain field in terms of the nodal displacement vector $\mathbf{q}$, we should transform the independent strain components from the element-fixed local orthogonal coordinate system back to the Cartesian coordinate system in order to compute the stiffness matrix.

$$\boldsymbol{\varepsilon}^{In} = \mathbf{T}\hat{\boldsymbol{\varepsilon}}^{In} = \mathbf{T}\mathbf{A}(\xi^\gamma)\mathbf{C}\mathbf{q} = \mathbf{T}\hat{\mathbf{B}}^*\mathbf{q} = \mathbf{B}^*\mathbf{q} \tag{45}$$

Thus the stiffness matrix can be computed as in equation (25):

$$\mathbf{K}^e = \int_{\Omega_m} \mathbf{B}^{*T}(\xi^\gamma)\mathbf{D}\mathbf{B}^*(\xi^\gamma)d\Omega = \mathbf{C}^T \int_{\Omega_m} \mathbf{A}^T(\xi^\gamma)\,\mathbf{T}^T\mathbf{D}\mathbf{T}\,\mathbf{A}(\xi^\gamma)d\Omega\,\mathbf{C} = \mathbf{C}^T\mathbf{K}^{ep}\,\mathbf{C} \tag{46}$$

Where

$$\mathbf{K}^{ep} = \int_{\Omega_m} \mathbf{A}^T(\xi^\gamma)\hat{\mathbf{D}}\mathbf{A}(\xi^\gamma)d\Omega \quad \text{and} \quad \hat{\mathbf{D}} = \mathbf{T}^T\mathbf{D}\mathbf{T} \tag{47}$$

So, in order to calculate the element stiffness matrix for the HMFEM-2 family, we use the transformation matrix $\mathbf{T}$ to obtain $\hat{\mathbf{D}} = \mathbf{T}^T\mathbf{D}\mathbf{T}$, then we use $\mathbf{A}(\xi^\gamma)$ to calculate $\mathbf{K}^{ep}$ and finally we use $\mathbf{C}$ to obtain $\mathbf{K}^e = \mathbf{C}^T\mathbf{K}^{ep}\,\mathbf{C}$, where $\mathbf{A}(\xi^\gamma)$ and $\mathbf{C}$ are defined in equation (44). The same procedure is followed for all the elements of

this HMFEM-2 family but using the corresponding representation of the **T** matrix, which depends on the shape functions of the element and the selected element-fixed local orthogonal base vectors, and the $\mathbf{A}(\xi^{\gamma})$ matrix which depends on the selected form of the independently assumed strain field. The matrix **C** depends on these previously mentioned selections.

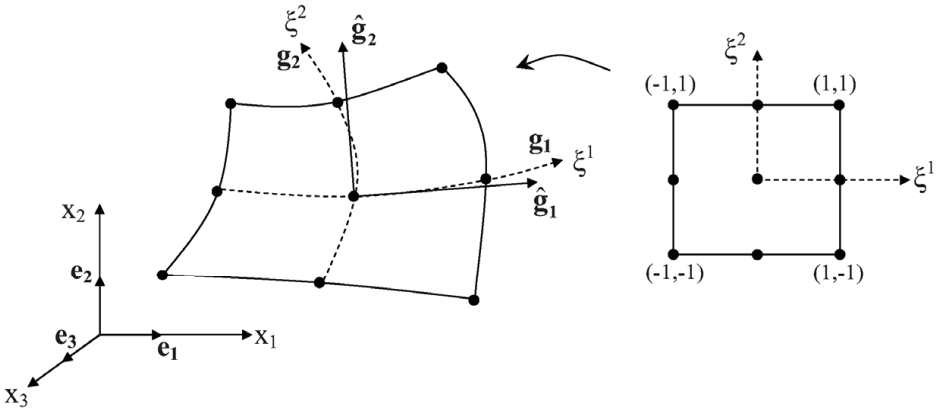

Figure 3: Global Cartesian coordinates, curvilinear coordinates, and element-fixed orthogonal base vectors for the nine-node quadrilateral finite element

3.2 Nine-node H/M Quadrilateral Element

Figure 3 shows the nine-node quadrilateral element in global Cartesian coordinates $x_1 - x_2 - x_3$ in the direction of the orthogonal base vectors $\mathbf{e_1} - \mathbf{e_2} - \mathbf{e_3}$, the element-fixed curvilinear coordinates $\xi^1 - \xi^2$, and the covariant base vectors $\mathbf{g_1} - \mathbf{g_2}$ in their directions, and the element-fixed local orthogonal base vectors $\hat{\mathbf{g}}_\mathbf{1} - \hat{\mathbf{g}}_\mathbf{2}$. The iso-parametric mapping transforms the regular element in the non-dimensional co-ordinates $\xi^1 - \xi^2$ that varies from -1 to 1 into the irregular element in the Cartesian $x_1 - x_2$ coordinates.

The same procedure used with the eight-node element is followed here. Collocation is also done by equating the two strain fields at the 9 points of the 3×3 Gauss quadrature points for the normal strains (points 10 to 18 in Figure 4 (left)), while at the 4 corner nodes of the 2×2 Gauss quadrature points (points 19 to 22 in Figure 4 (right)) for the shear strains.

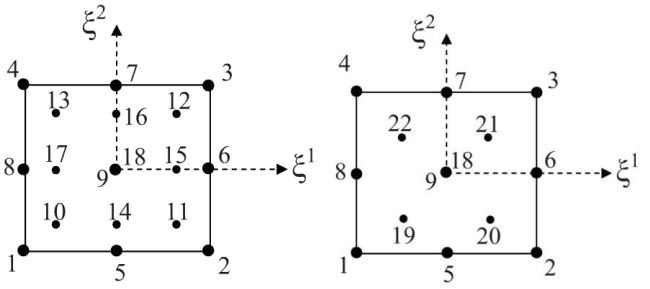

Figure 4: The nine-node quadrilateral element in the non-dimensional coordinate system with the 3×3 (left) and 2×2 (right) Gauss quadrature points

3.3 Numerical Examples

In order to test the performance of the new elements, some numerical tests will be illustrated here. The properties that will be tested are: stiffness, invariance, stability and efficiency, patch test, Locking, and sensitivity to mesh distortion.

3.3.1 Stiffness, Invariance, Stability and Efficiency

A single square element is considered here, with 8-nodes having Cartesian coordinates: (-1,-1), (1,-1), (1,1), (-1,1), (0,-1), (1,0), (0,1), (-1,0) with the addition of the center node (0,0) for the case of the nine-node elements. The material properties are: E = 1 and $\nu = 0.25$. The eigenvalues of the element in Cartesian coordinates are computed to compare the stiffness of the HMFEM-2 higher order two-dimensional elements with the primal displacement-based finite elements (DPFEM). Then the global Cartesian coordinate system is rotated counterclockwise by any arbitrary angle θ and the eigenvalues are computed again in order to check the invariance property. Finally the CPU time is recorded for all the cases to compare the efficiency.

Figure 5 shows the configuration of the test. Table 1 shows the eigenvalues of the different higher order elements. It can be seen that, first, all the elements are stable because only three zero eigenvalues exist for each element corresponding to the three rigid-body modes. Second, the new HMFEM-2 elements are less stiff than the DPFEM elements (some of the eigenvalues are smaller for the HMFEM-2 than their correspondents in the DPFEM, especially for the nine-node elements). This is a desirable property that resulted from the unlocked nature of the new elements. However, the "limitation principle" resulted in the fact that the present 8-noded HMFEM-2 is not significantly better than the 8-noded DPFEM.

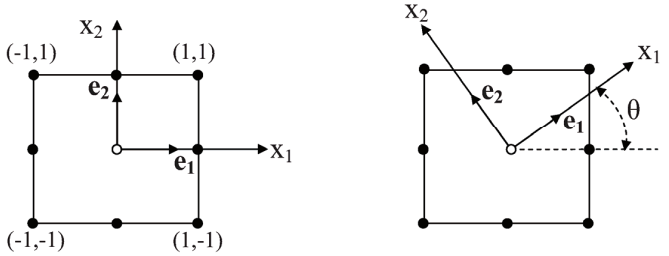

Figure 5: Test of invariance under coordinate system rotation

Exactly the same eigenvalues were obtained when the original coordinate system is rotated counterclockwise by any arbitrary angle θ (See Figure 5). The DPFEM is known to be invariant while the invariance of the HMFEM-2 elements is a result of using the element-fixed local orthogonal coordinate system introduced before. Thus, the new elements are invariant. It is worth mentioning that all these elements are invariant whatever the shape or the distortion of the element. If we used an arbitrary quadrilateral element (not of a rectangular shape), the elements will stay invariant for any rotation of the original coordinate system.

Finally, the CPU time required to compute the stiffness matrix for each element is presented in Table 2, and is normalized to the case of the DPFEM elements in the last row. It can be seen that the HMFEM-2 elements are not as efficient as that of the DPFEM cases because of the extra computation needed for transformation between ε_{ij} and $\hat{\varepsilon}^{kl}$ and between $\hat{\varepsilon}^{Inij}$ and ε^{In}_{kl}, and for computing the strain field derived from the displacement field in order to collocate it with the independent strain field.

From Table 1 and Table 2, it is evident that the present hybrid/mixed formulation using non-locking independently assumed strains, and compatible displacements does not improve the performances of the 8- and 9-noded 2D quadrilateral elements significantly, due to the "limitation principle", even though the computational cost of the present hybrid/mixed element is still higher than that of the pure displacement element. However, it was shown in [Dong and Atluri (2011a)] that the lower-order 4-node quadrilateral HMFEM-2 element, performs much better than the displacement based DPFEM 4-node quadrilateral element, and this is also the case for the lower-order 8-node 3D brick element that will be presented in the next section of this paper. Also, it should be pointed out that since no element-computation of other supplementary matrices $\mathbf{H}$ and $\mathbf{G}$, and their inversions are involved in the present mixed formulation, the computation of the element stiffness matrix is much cheaper and more efficient than that of the elements formulated by

Table 1: Eigenvalues of the stiffness matrix of different elements in the original Cartesian coordinate system

Eigenvalue	Elements			
	DPFEM-Q8	HMFEM-2 (Q8)	DPFEM-Q9	HMFEM-2 (Q9)
1	0	0	0	0
2	0	0	0	0
3	0	0	0	0
4	0.165	0.165	0.165	0.165
5	0.3015	0.3015	0.2725	0.2659
6	0.3015	0.3015	0.2725	0.2659
7	0.4497	0.4444	0.4497	0.4444
8	0.5673	0.5673	0.5673	0.5408
9	0.9195	0.9195	0.6712	0.5408
10	1.1733	1.0667	0.6712	0.5673
11	1.4602	1.4602	0.9195	0.9195
12	1.4602	1.4602	1.1733	1.0667
13	2.1172	2.1172	1.6129	1.5611
14	2.2347	2.1333	1.6129	1.5611
15	4.5938	4.5938	2.1172	2.1172
16	4.5938	4.5938	2.2347	2.1333
17			5.3634	5.1255
18			5.3634	5.1255

Table 2: CPU time (in seconds) required for computing the stiffness matrix of each element, normalized to that of the DPFEM elements in the last row

CPU Time	Element			
	DPFEM-Q8	HMFEM-2 (Q8)	DPFEM-Q9	HMFEM-2 (Q9)
	0.000668	0.0011	0.000655	0.0012
	1	1.646706587	1	1.832061069

multi-field variational principles [Pian (1964); Punch and Atluri (1984a); Punch and Atluri (1984b); Pian and Wu (1983)].

3.3.2 Patch test

Patch test requires that any arbitrary linear displacement field can theoretically be exactly reproduced by using a small number of elements in the patch.

A standard stress patch test is shown in Figure 6. A square sheet of side length

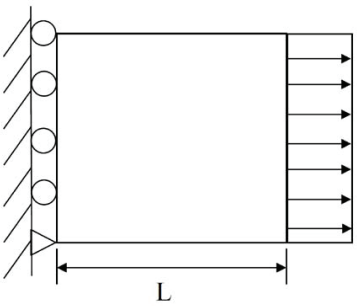

Figure 6: Patch test: a cube under constant tensile stress or uniform displacement

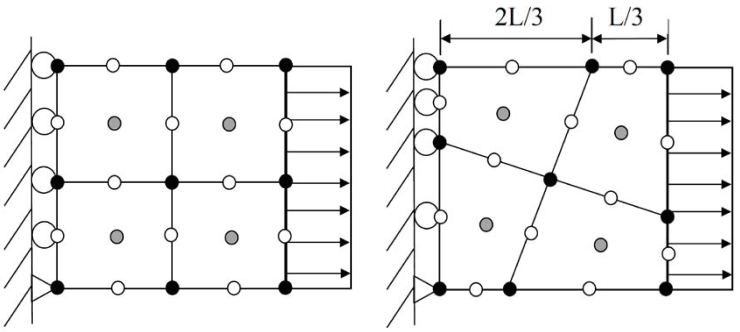

Figure 7: Two mesh configurations for the patch test

"L" fixed from one side and is subjected to uniform tensile stress as shown in the figure. The square domain is meshed using 4 two-dimensional elements, once in a regular configuration and again in an irregular configuration as shown in Figure 7. The geometrical properties of this problem is L = 1, while the material properties are: E = 1 and ν= 0.25.

This problem has a simple analytical solution and thus the error can be defined as:

$$Error = \frac{\|\mathbf{q} - \mathbf{q}^{exact}\|}{\|\mathbf{q}^{exact}\|} \tag{48}$$

Where $\mathbf{q}$ and $\mathbf{q}^{exact}$ are the computed and exact nodal displacement vector. $\|\|$ represents the 2-norm.

Table 3 shows the errors for all the elements for the cases of regular and irregular meshes. The errors are very small for all the elements and thus, all pass the constant stress patch test.

Table 3: Performance of different elements in the constant stress patch test

Mesh	DPFEM-Q8	HMFEM-2 (Q8)	DPFEM-Q9	HMFEM-2 (Q9)
Regular	6.9797×10^{-15}	2.0892×10^{-15}	3.7777×10^{-15}	3.9070×10^{-15}
Irregular	3.6440×10^{-15}	2.9436×10^{-15}	1.7293×10^{-15}	2.0309×10^{-15}

Considering a displacement patch test, and instead of applying a uniform stress field on the plate in Figure 6, a uniform displacement is applied and the displacement of the center point of the plate is compared to the exact solution. This time the error is defined as:

$$Error = \frac{|u_c - u_c^{exact}|}{|u_c^{exact}|} \tag{49}$$

Where u_c and u_c^{exact} are the computed and the exact center point displacements respectively.

Table 4 shows the errors for all the elements for the cases of regular and irregular meshes. The errors are very small for all the elements and thus, all pass the uniform displacement patch test.

Table 4: Performance of different elements in the uniform displacement patch test

Mesh	DPFEM-Q8	HMFEM-2 (Q8)	DPFEM-Q9	HMFEM-2 (Q9)
Regular	2.5403×10^{-15}	1.6212×10^{-15}	1.0401×10^{-15}	1.0824×10^{-15}
Irregular	5.4920×10^{-15}	5.1161×10^{-15}	5.8252×10^{-15}	7.5395×10^{-15}

3.3.3 Locking

In order to test the performance of the elements against locking, a plane stress problem in the form of a cantilevered 2D beam of length L, width W = 2c and unit thickness, subjected to an end load as shown in Figure 8 is considered. The beam is composed of five elements with different distortions in each of them as used by [Pian and Sumihara (1984)].

For this test, the geometric properties are L = 10, c = 1, and the material properties are E = 1500, and ν= 0.25. Two loading cases are considered: end shear with P = 300 and end moment with M = 2000. Table 5 shows the computed tip vertical displacement at point "A" and the computed normal stress at the lower left Gaussian point "B" of the leftmost element. The table also shows the results of the exact theory of elasticity model.

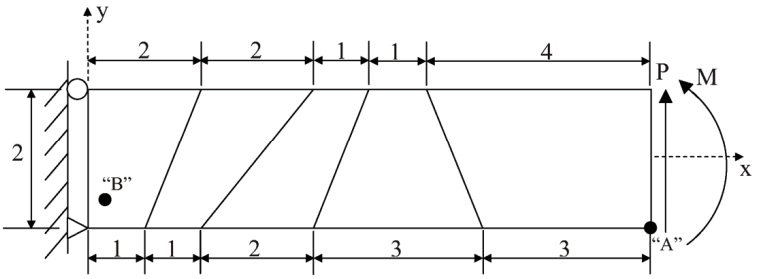

Figure 8: Mesh configuration for overall test of performance against locking

The exact solution of this problem can be found in [Timoshenko and Goodier (1976)] as:

End Shear loading:

$$\begin{aligned}
u_x &= -\frac{Py}{6\bar{E}I}[3x(2L-x)+(2+\bar{\nu})(y^2-c^2)] \\
u_y &= \frac{P}{6\bar{E}I}[x^2(3L-x)+3\bar{\nu}(L-x)y^2+(4+5\bar{\nu})c^2x] \\
\sigma_x &= -\frac{P}{I}(L-x)y \\
\sigma_y &= 0 \\
\sigma_{xy} &= -\frac{P}{2I}(y^2-c^2)
\end{aligned} \tag{50}$$

End Bending loading:

$$\begin{aligned}
u_x &= -\frac{M}{\bar{E}I}xy \\
u_y &= \frac{M}{2\bar{E}I}(x^2+\bar{\nu}y^2) \\
\sigma_x &= -\frac{M}{I}y \\
\sigma_y &= -\frac{\bar{\nu}}{1-\bar{\nu}^2}\frac{M}{I}y \\
\sigma_{xy} &= 0
\end{aligned} \tag{51}$$

Where

$$I=\frac{2c^3}{3} \quad \bar{E}=\begin{cases} E & \\ \frac{E}{(1-\nu)^2} & \end{cases} \qquad \bar{\nu}=\begin{cases} \nu & \text{for plane stress} \\ \frac{\nu}{(1-\nu)} & \text{for plane strain} \end{cases} \tag{52}$$

Table 5: Computed and Exact solutions of cantilever beam under end shear or end moment

Element type	End Shear		End Bending	
	v_A	σ_b	v_A	σ_b
DPFEM-Q8	101.8345	2512.2	99.9179	1731.8
HMFEM-2 (Q8)	102.2350	2528.6	99.9780	1731.2
DPFEM-Q9	102.3742	2523.3	100.25	1732.1
MHFEM-2 (Q9)	102.7707	2532.3	100.25	1732.1
Exact	102.625	2531.8	100.3	1732.1

As explained before, for the quadrilateral 8 and 9-noded plane elements, the present formulation does not significantly improve the performance of the elements formulated by the usual primal method because of the "limitation principle".

3.3.4 Sensitivity to element distortion

In order to test the sensitivity of the elements to mesh distortion, the same plane stress problem can be used, but this time the cantilever beam will be composed of only two distorted elements as shown in Figure 9. The distortion ratio is defined as 2e/L. the geometrical properties for this test is: L = 10 and c = 1, while the material properties are: E = 1 and $\nu = 0$.

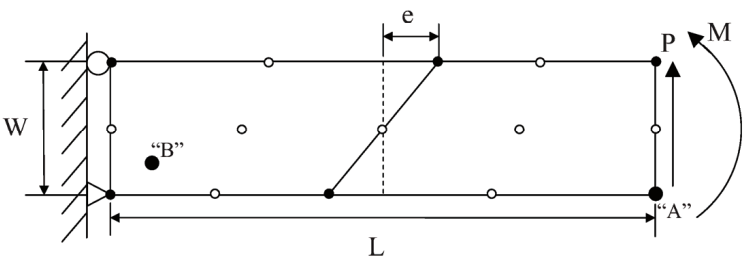

Figure 9: Test of element sensitivity to element distortion, cantilever beam under end loading

Figure 10 shows the effect of varying the distortion ratio on the computed relative stress and the computed relative displacement (FE/Exact) for the eight-node elements for the case of end shear, while Figure 11 shows that for the end bending case. Figure 12 and Figure 13 show the same plots but for the nine-node elements.

It can be seen from Figure 10 to Figure 13 that the sensitivity to element distortion of the HMFEM-2 elements is always less than or equal that of the DPFEM ele-

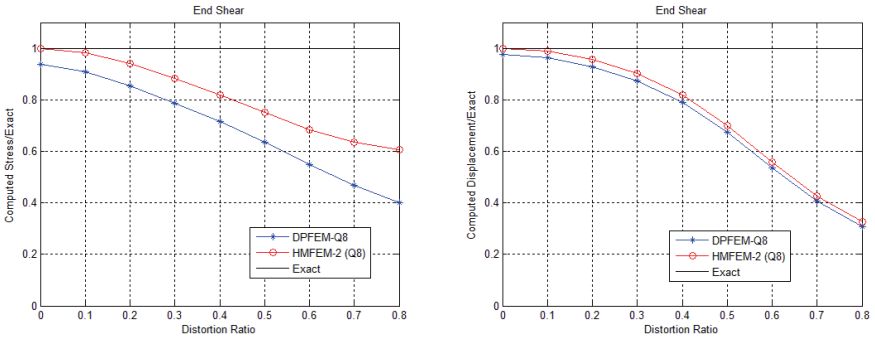

Figure 10: Relative stress at point "B" and relative displacement at point "A" for the 2D 8-node elements for end shear load case

ments. It is also clear that the nine-node elements give significantly more accurate results than those of the eight-node elements.

4 Isoparametric three-dimensional Hybrid/Mixed brick elements

4.1 Eight-node H/M Brick Element

Figure 14 shows the eight-node brick element in global Cartesian coordinates $x_1 - x_2 - x_3$ in the direction of the orthogonal base vectors $\mathbf{e_1} - \mathbf{e_2} - \mathbf{e_3}$, the element-fixed curvilinear coordinates $\xi^1 - \xi^2 - \xi^3$, and the covariant base vectors $\mathbf{g_1} - \mathbf{g_2} - \mathbf{g_3}$ in their directions, and the element-fixed local orthogonal base vectors $\hat{\mathbf{g}}_\mathbf{1} - \hat{\mathbf{g}}^\mathbf{2} - \hat{\mathbf{g}}_\mathbf{p}$. The isoparametric mapping transforms the regular element in the non-dimensional coordinates $\xi^1 - \xi^2 - \xi^3$ that varies from -1 to 1 into the irregular element in the Cartesian $x_1 - x_2 - x_3$ coordinates.

The element-fixed local orthogonal base vectors $\hat{\mathbf{g}}_\mathbf{1} - \hat{\mathbf{g}}^\mathbf{2} - \hat{\mathbf{g}}_\mathbf{p}$ are defined as follows: $\hat{\mathbf{g}}_\mathbf{1}$ is in the same direction of the covariant base vector $\mathbf{g_1}$ evaluated at the center (0, 0, 0), $\mathbf{g^2}$ is the contravariant base vector perpendicular to $\mathbf{g_1}$ and $\mathbf{g_3}$ (i.e. $\mathbf{g^2} = \mathbf{g_3} \times \mathbf{g_1}$) and $\hat{\mathbf{g}}^\mathbf{2}$ is in the same direction of $\mathbf{g^2}$ but evaluated at the center (0, 0, 0), and finally $\hat{\mathbf{g}}_\mathbf{p}$ is perpendicular to both $\hat{\mathbf{g}}_\mathbf{1}$ and $\hat{\mathbf{g}}^\mathbf{2}$.

Following the same procedure illustrated in the two-dimensional case, but using the

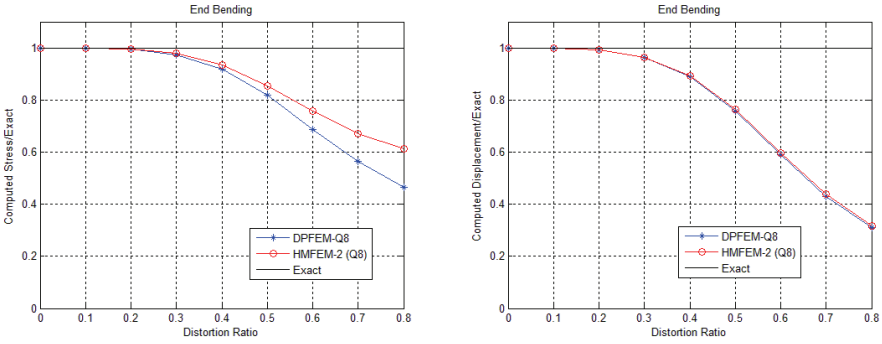

Figure 11: Relative stress at point "B" and relative displacement at point "A" for the 2D 8-node elements for end bending load case

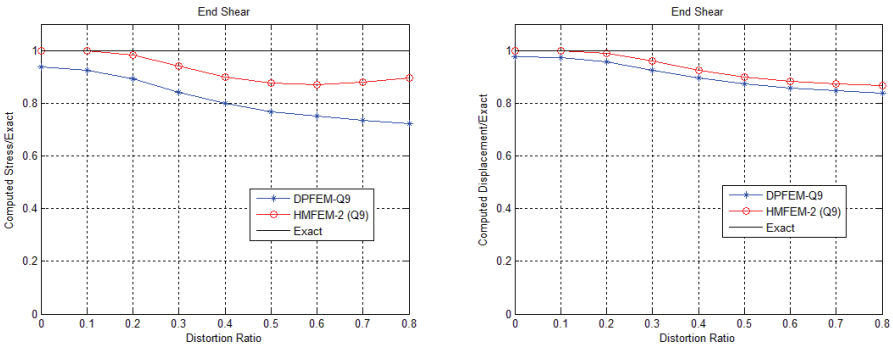

Figure 12: Relative stress at point "B" and relative displacement at point "A" for the 2D 9-node elements for end shear load case

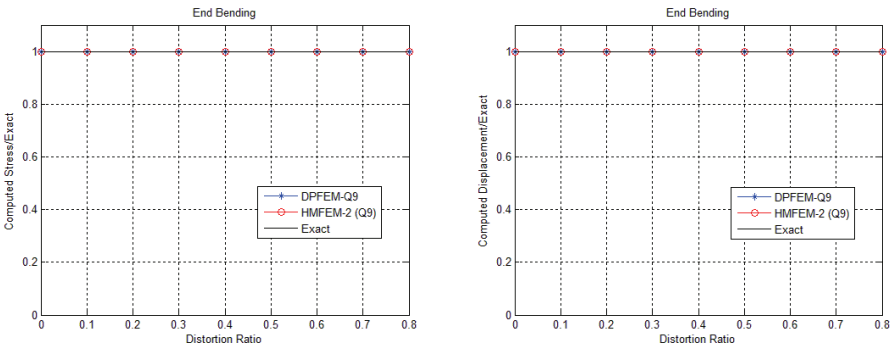

Figure 13: Relative stress at point "B" and relative displacement at point "A" for the 2D 9-node elements for end bending load case

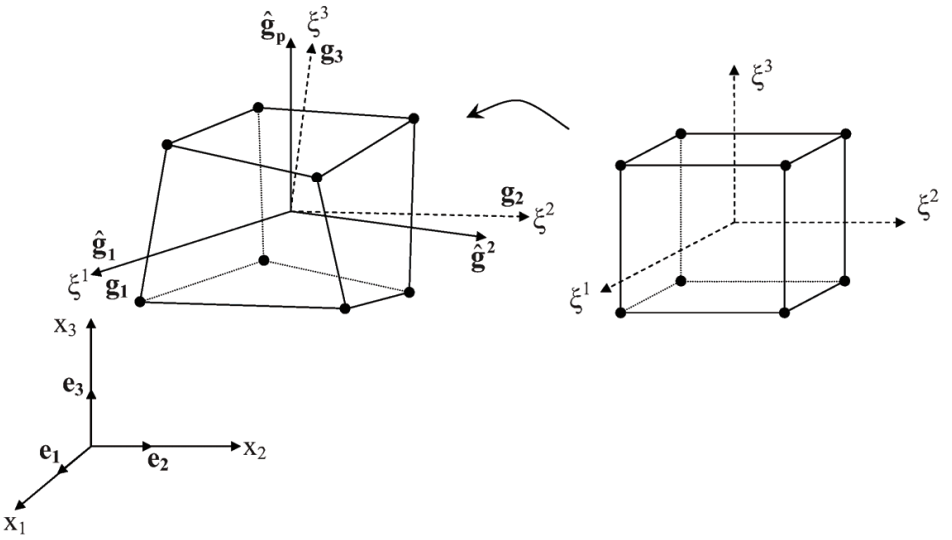

Figure 14: Global Cartesian coordinates, curvilinear coordinates, and element-fixed orthogonal base vectors for the eight-node brick finite element

independent strain components as:

$$\begin{aligned}
\hat{\varepsilon}^{In11} &= \alpha_1 + \alpha_2\xi^2 + \alpha_3\xi^3 + \alpha_4\xi^2\xi^3 \\
\hat{\varepsilon}^{In22} &= \alpha_5 + \alpha_6\xi^1 + \alpha_7\xi^3 + \alpha_8\xi^1\xi^3 \\
\hat{\varepsilon}^{In33} &= \alpha_9 + \alpha_{10}\xi^1 + \alpha_{11}\xi^2 + \alpha_{12}\xi^1\xi^2 \\
\hat{\varepsilon}^{In12} &= \beta_1 + \beta_2\xi^3 \\
\hat{\varepsilon}^{In23} &= \beta_3 + \beta_4\xi^1 \\
\hat{\varepsilon}^{In31} &= \beta_5 + \beta_6\xi^2
\end{aligned} \tag{53}$$

Note that the shear strains are completely decoupled from the direct strains, and also the shear strains are of lower order as compared to the direct strains. Also note that the presently chosen least-order strain field in each element is physically motivated as: the direct strain in each direction involves linear strains in the other two directions, correctly reflecting the bending modes. There are a total of 18 independently assumed, and judiciously chosen strain parameters in this 8-noded brick element with 24 displacement degrees of freedom and 6 rigid-body modes. Thus the chosen independent strain field is of the least order possible.

This can be written as in equation (9):

$$\hat{\varepsilon}^{In11} = \mathbf{A_1}(\xi^\gamma)\boldsymbol{\alpha_1}\,, \quad \hat{\varepsilon}^{In12} = \mathbf{A_{s1}}(\xi^\gamma)\boldsymbol{\beta_1}, \text{ etc..} \tag{54}$$

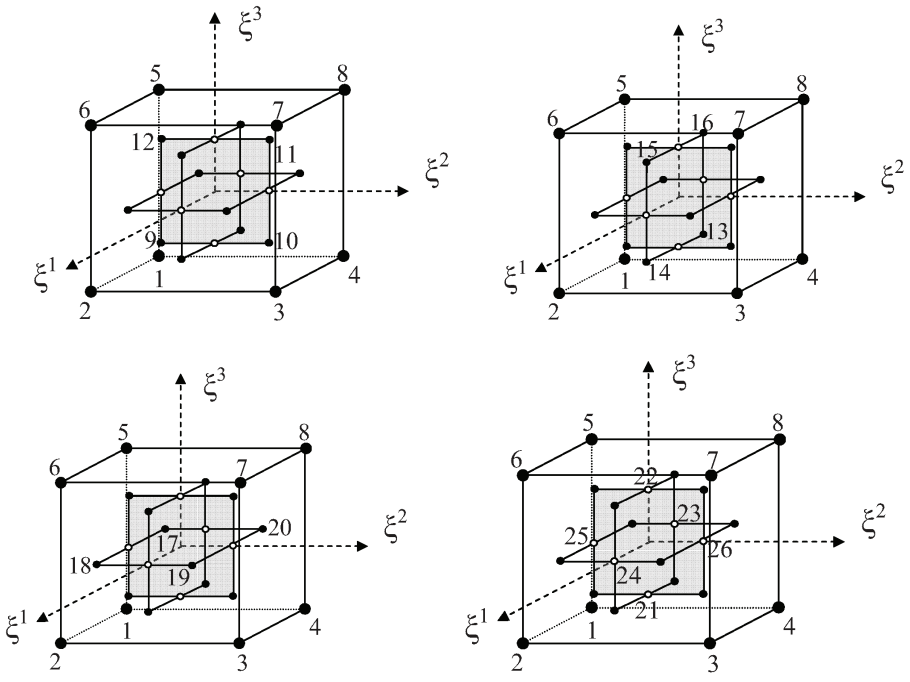

Figure 15: The eight-node brick element in the non-dimensional coordinates and the different collocation points

Where:

$$\mathbf{A_1}(\xi^\gamma) = \begin{bmatrix} 1 & \xi^2 & \xi^3 & \xi^2\xi^3 \end{bmatrix}$$

$$\boldsymbol{\alpha}_1 = \begin{bmatrix} \alpha_1 & \alpha_2 & \alpha_3 & \alpha_4 \end{bmatrix}^T$$

$$\mathbf{A_{s1}}(\xi^\gamma) = \begin{bmatrix} 1 & \xi^3 \end{bmatrix}$$

$$\boldsymbol{\beta_1} = \begin{bmatrix} \beta_1 & \beta_2 \end{bmatrix}$$

$\boldsymbol{\alpha_i}, \boldsymbol{\beta_i}$, $i = 1-3$ are vectors of undetermined parameters.

Collocation is done by equating the normal strains of the two strain fields at only 4 points from the $2\times2\times2$ Gauss quadrature points, and these 4 points are not the

same for each of the 3 normal strain components. $\hat{\varepsilon}^{In11}$ components are collocated at the 4 Gauss quadrature points at the corners of the hatched plane in Figure 15 (upper left) having $\xi^1 = 0$ (points 9-12). While $\hat{\varepsilon}^{In22}$ are collocated at the 4 corners of the plane having $\xi^2 = 0$ (points 13-16 in Figure 15 (upper right)), and $\hat{\varepsilon}^{In33}$ are collocated at the 4 corners of the plane having $\xi^3 = 0$ (points 17-20 in Figure 15 (lower left)). Each of the shear strain components are also collocated at different points. $\hat{\varepsilon}^{In12}$ components are collocated at the 2 Gaussian points with $\xi^1 = \xi^2 = 0$ (points 21-22 in Figure 15 (lower right)), $\hat{\varepsilon}^{In23}$ are collocated at the 2 Gaussian points with $\xi^2 = \xi^3 = 0$ (points 23-24 in Figure 15 (lower right)), and finally $\hat{\varepsilon}^{In31}$ are collocated at the 2 Gaussian points with $\xi^1 = \xi^3 = 0$ (points 25-26 in Figure 15 (lower right)).

The following alternative choice of the independent strain field can also lead to a more efficient element:

$$\begin{aligned}
\hat{\varepsilon}^{In11} &= \alpha_1 + \alpha_2\xi^1 + \alpha_3\xi^2 + \alpha_4\xi^3 + \alpha_5\xi^1\xi^2 + \alpha_6\xi^2\xi^3 + \alpha_7\xi^1\xi^3 + \alpha_8\xi^1\xi^2\xi^3 \\
\hat{\varepsilon}^{In22} &= \alpha_9 + \alpha_{10}\xi^1 + \alpha_{11}\xi^2 + \alpha_{12}\xi^3 + \alpha_{13}\xi^1\xi^2 + \alpha_{14}\xi^2\xi^3 + \alpha_{15}\xi^1\xi^3 + \alpha_{16}\xi^1\xi^2\xi^3 \\
\hat{\varepsilon}^{In33} &= \alpha_{17} + \alpha_{18}\xi^1 + \alpha_{19}\xi^2 + \alpha_{20}\xi^3 + \alpha_{21}\xi^1\xi^2 + \alpha_{22}\xi^2\xi^3 + \alpha_{23}\xi^1\xi^3 + \alpha_{24}\xi^1\xi^2\xi^3 \\
\hat{\varepsilon}^{In12} &= \beta_1 + \beta_2\xi^3 \\
\hat{\varepsilon}^{In23} &= \beta_3 + \beta_4\xi^1 \\
\hat{\varepsilon}^{In31} &= \beta_5 + \beta_6\xi^2
\end{aligned} \tag{55}$$

giving a total of 30 independent strain modes in the 8-noded brick element.

The collocation is done at the 8 points of the 2×2×2 Gaussian points (points 9-16 in Figure 16) for all the normal strain components, while the shear strains are collocated in the same fashion mentioned before (see Figure 15 (lower right) and the preceding paragraph). Using this choice of strain field and collocation points, even though includes more terms in the normal strain components, is efficient since the collocation points are the same quadrature points that are used in integrating the stiffness matrix (using 2×2×2 Gauss quadrature rule). However, the two mentioned choices of strain fields, i.e. equation (53) and (55) respectively, with their associated collocation points yield the same element (same stiffness matrix).

4.2 Twenty-node H/M Quadratic Brick Element

Figure 17 shows the twenty-node quadratic brick element, and the different coordinate systems and base vectors involved in the transformations.

The same procedure will be followed here as in the eight node brick element case,

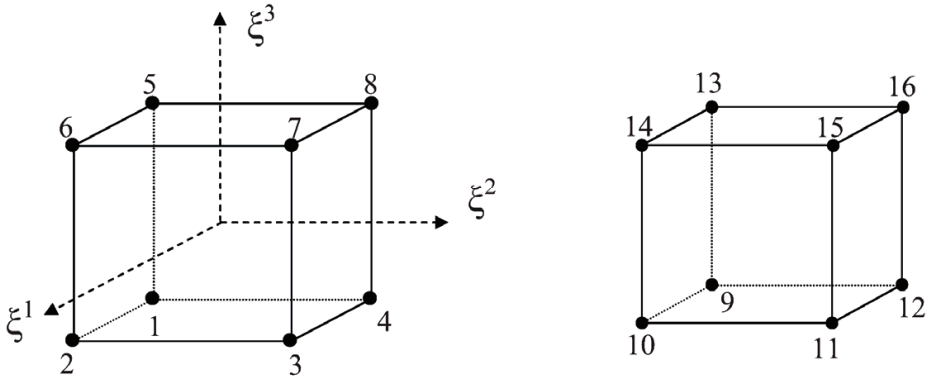

Figure 16: The eight-node brick element in the non-dimensional coordinates and the 2×2×2 Gauss quadrature points which are the collocation points for the normal strain components (Extracted from the element for illustration)

but the independent strain components have the form:

$$
\begin{aligned}
\hat{\varepsilon}^{I11} &= \alpha_1 + \alpha_2\xi^1 + \alpha_3\xi^2 + \alpha_4\xi^3 + \alpha_5\xi^1\xi^2 + \alpha_6(\xi^2)^2 + \alpha_7\xi^2\xi^3 + \alpha_8(\xi^3)^2 + \alpha_9\xi^1\xi^3 \\
&\quad + \alpha_{10}\xi^1(\xi^2)^2 + \alpha_{11}\xi^1(\xi^3)^2 + \alpha_{12}\xi^2(\xi^3)^2 + \alpha_{13}\xi^3(\xi^2)^2 + \alpha_{14}\xi^1\xi^2\xi^3 \\
&\quad + \alpha_{15}\xi^1\xi^2(\xi^3)^2 + \alpha_{16}\xi^1\xi^3(\xi^2)^2 \\
\hat{\varepsilon}^{I22} &= \alpha_{17} + \alpha_{18}\xi^1 + \alpha_{19}\xi^2 + \alpha_{20}\xi^3 + \alpha_{21}\xi^1\xi^2 + \alpha_{22}(\xi^1)^2 + \alpha_{23}\xi^2\xi^3 + \alpha_{24}(\xi^3)^2 \\
&\quad + \alpha_{25}\xi^1\xi^3 + \alpha_{26}\xi^2(\xi^1)^2 + \alpha_{27}\xi^2(\xi^3)^2 + \alpha_{28}\xi^1(\xi^3)^2 + \alpha_{29}\xi^3(\xi^1)^2 \\
&\quad + \alpha_{30}\xi^1\xi^2\xi^3 + \alpha_{31}\xi^2\xi^1(\xi^3)^2 + \alpha_{32}\xi^2\xi^3(\xi^1)^2 \\
\hat{\varepsilon}^{I33} &= \alpha_{33} + \alpha_{34}\xi^1 + \alpha_{35}\xi^2 + \alpha_{36}\xi^3 + \alpha_{37}\xi^1\xi^2 + \alpha_{38}(\xi^1)^2 + \alpha_{39}\xi^2\xi^3 + \alpha_{40}(\xi^2)^2 \\
&\quad + \alpha_{41}\xi^1\xi^3 + \alpha_{42}\xi^3(\xi^1)^2 + \alpha_{43}\xi^3(\xi^2)^2 + \alpha_{44}\xi^1(\xi^2)^2 + \alpha_{45}\xi^2(\xi^1)^2 \\
&\quad + \alpha_{46}\xi^1\xi^2\xi^3 + \alpha_{47}\xi^3\xi^2(\xi^1)^2 + \alpha_{48}\xi^3\xi^1(\xi^2)^2 \\
\hat{\varepsilon}^{I12} &= \beta_1 + \beta_2\xi^1 + \beta_3\xi^2 + \beta_4\xi^3 + \beta_5\xi^1\xi^2 + \beta_6\xi^2\xi^3 + \beta_7\xi^3\xi^1 + \beta_8\xi^1\xi^2\xi^3 \\
\hat{\varepsilon}^{I23} &= \beta_9 + \beta_{10}\xi^1 + \beta_{11}\xi^2 + \beta_{12}\xi^3 + \beta_{13}\xi^1\xi^2 + \beta_{14}\xi^2\xi^3 + \beta_{15}\xi^3\xi^1 + \beta_{16}\xi^1\xi^2\xi^3 \\
\hat{\varepsilon}^{I31} &= \beta_{17} + \beta_{18}\xi^1 + \beta_{19}\xi^2 + \beta_{20}\xi^3 + \beta_{21}\xi^1\xi^2 + \beta_{22}\xi^2\xi^3 + \beta_{23}\xi^3\xi^1 + \beta_{24}\xi^1\xi^2\xi^3
\end{aligned}
\tag{56}
$$

This can be written as in equation (9):

$$
\hat{\varepsilon}^{In11} = \mathbf{A_1}(\xi^\gamma)\boldsymbol{\alpha_1}, \quad \hat{\varepsilon}^{In12} = \mathbf{A_{s1}}(\xi^\gamma)\boldsymbol{\beta_1}, \text{ etc..} \tag{57}
$$

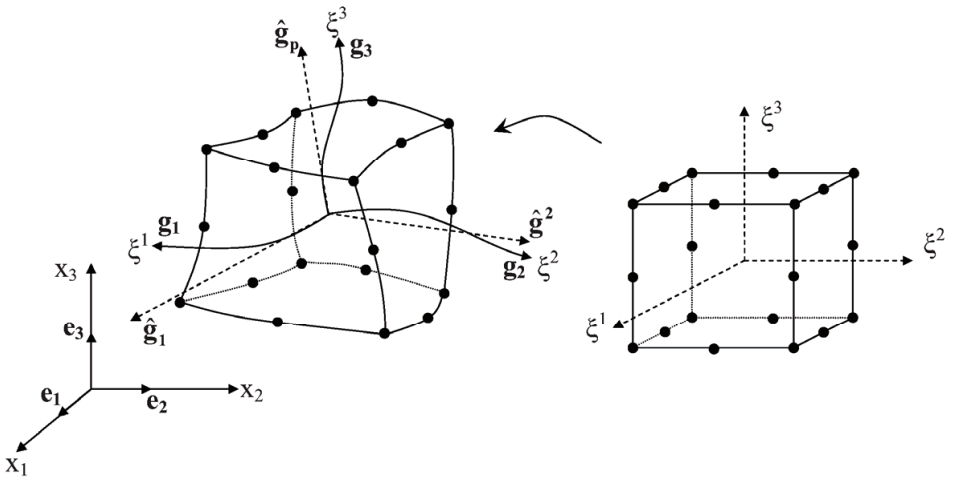

Figure 17: Global Cartesian coordinates, curvilinear coordinates, and element-fixed orthogonal base vectors for the twenty-node brick finite element

Where:

$$\mathbf{A_1}(\xi^\gamma) = \begin{bmatrix} 1 & \xi^1 & \xi^2 & \xi^3 & \xi^1\xi^2 & (\xi^2)^2 & \xi^2\xi^3 & (\xi^3)^2 & \xi^1\xi^3 & \xi^1(\xi^2)^2 \\ & \xi^1(\xi^3)^2 & \xi^2(\xi^3)^2 & \xi^3(\xi^2)^2 & \xi^1\xi^2\xi^3 & \xi^1\xi^2(\xi^3)^2 & \xi^1\xi^3(\xi^2)^2 & \end{bmatrix}$$

$$\boldsymbol{\alpha_1} = \begin{bmatrix} \alpha_1 & \ldots & \alpha_{16} \end{bmatrix}^T$$

$$\mathbf{A_{s1}}(\xi^\gamma) = \begin{bmatrix} 1 & \xi^1 & \xi^2 & \xi^3 & \xi^1\xi^2 & \xi^2\xi^3 & \xi^3\xi^1 & \xi^1\xi^2\xi^3 \end{bmatrix}$$

$$\boldsymbol{\beta_1} = \begin{bmatrix} \beta_1 & \ldots & \beta_8 \end{bmatrix}$$

$\boldsymbol{\alpha_i}$, $\boldsymbol{\beta_i}$, i=1-3 are vectors of undetermined parameters.

Collocation is done by equating the two strain fields at 16 points of the 3×3×3 Gauss quadrature points for the normal strains, but these 16 points are not the same for the three normal strains. Figure 18 (right) shows the 27 points of the 3×3×3 Gauss quadrature points, extracted from the 20 node brick element for clarification. $\hat{\varepsilon}^{In11}$ components are collocated at points 21-24, 26-29, 39-42 and 44-47 in Figure

18 (right). $\hat{\varepsilon}^{In22}$ are collocated at points 21, 23, 24, 26, 27, 29, 30, 32, 36, 38, 39, 41, 42, 44, 45, and 47 in Figure 18 (right). $\hat{\varepsilon}^{In33}$ are collocated at points 21-23, 27-29, 30, 32, 36, 38, 39-41, and 45-47 in Figure 18 (right).

While all the shear strain components are collocated at the 8 corner points of the 3×3×3 Gauss quadrature points (points 21, 23, 27, 29, 39, 41, 45 and 47 in Figure 18 (right)). Selecting these 8 points for collocating the shear strain components is more efficient than selecting the 8 corner points of the 2×2×2 Gauss quadrature points since the selected points belong to the quadrature points used in integrating the stiffness matrix (3×3×3 Gauss quadrature rule), so no need for more computations to collocate at other points.

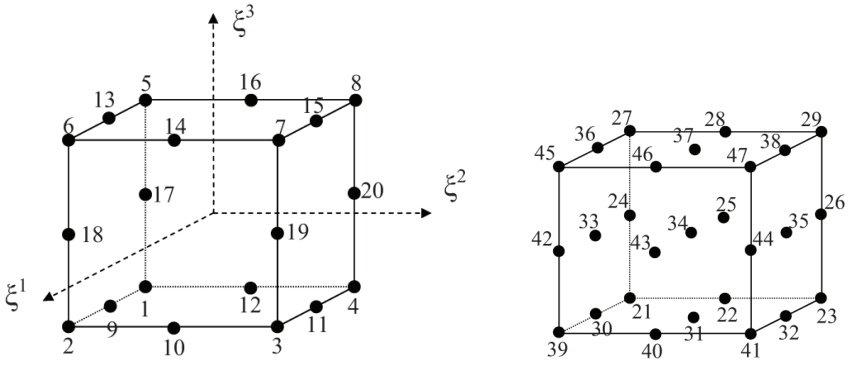

Figure 18: (left): The twenty-node brick element, (right): 3×3×3 Gaussian points

4.3 Numerical Examples

4.3.1 Stiffness, Invariance, Stability and Efficiency

A single cube element is considered here, with its 8 corners having Cartesian coordinates: (-1,-1,-1), (1,-1,-1), (1,1,-1), (-1,1,-1), (-1,-1,1), (1,-1,1), (1,1,1), (-1,1,1). The material properties are: E = 1 and ν= 0.25. The eigenvalues of the element in Cartesian coordinates are computed to compare the stiffness of the HMFEM-2 three-dimensional elements with the primal displacement-based finite elements (DPFEM). Then the global Cartesian coordinate system is rotated counterclockwise by any arbitrary angle θ once around the ξ^1axis, then around ξ^2 axis and again around ξ^3axis. After each rotation, the eigenvalues are computed in order to check the invariance property. Finally the CPU time is recorded for all the cases to compare the efficiency.

Table 6 shows the eigenvalues of the different 3D 8-noded "linear" brick elements, while Table 7 shows that of the different 20-noded brick elements. It can be seen that, first all the elements are stable because only six zero eigenvalues exist for each element corresponding to the six rigid-body modes. Second, the new HMFEM-2 elements are significantly less stiff than the DPFEM elements (the values of the eigenvalues are smaller for the HMFEM-2). This is a desirable property that resulted from the unlocked nature of the new elements.

It is thus seen that the present HMFEM-2 formulation improves significantly the performance of the lower order 8-noded linear brick elements, as compared to the pure displacement formulation.

Table 6: Eigenvalues of the stiffness matrix of the eight-node brick elements in the original coordinate system

Eigenvalue	Elements				
	DPFEM-B8	HMFEM-2 (B8)		DPFEM-B8	HMFEM-2 (B8)
1	0	0	13	0.4	0.2667
2	0	0	14	0.4	0.2667
3	0	0	15	0.5333	0.5333
4	0	0	16	0.6667	0.5333
5	0	0	17	0.6667	0.5333
6	0	0	18	0.6667	0.5333
7	0.1333	0.1333	19	0.8	0.8
8	0.1333	0.1333	20	0.8	0.8
9	0.2222	0.1333	21	0.8	0.8
10	0.2222	0.1333	22	0.8	0.8
11	0.2222	0.1333	23	0.8	0.8
12	0.4	0.2667	24	2	2

Exactly the same eigenvalues were obtained when the original coordinate system is rotated counterclockwise around any coordinate axis. The DPFEM is known to be invariant while the invariance of the HMFEM-2 elements is a result of using the element-fixed local orthogonal coordinate system introduced before. Thus, the new elements are invariant. It is worth mentioning that all these elements are invariant whatever the shape or the distortion of the element. If we used an arbitrary hexahedron element (not of a cubic shape), the elements will stay invariant for any rotation of the original coordinate system.

Finally, the CPU time required to compute the stiffness matrix for each element is presented in Table 8, and is normalized to the case of the DPFEM elements in the

last row. It can be seen that the HMFEM-2 elements are not as computationally efficient as that of the DPFEM cases because of the extra computation needed for transformation between ε_{ij} and $\hat{\varepsilon}^{kl}$ and between $\hat{\varepsilon}^{Inij}$ and ε^{In}_{kl}, and for computing the strain field derived from the displacement field in order to collocate it with the independent strain field. As the order of the element is increased the difference in CPU time between the DPFEM and HMFEM-2 elements tends to decrease, but the performances of both types of elements tend to be similar as will be illustrated in thefollowing examples in the section. The HMFEM-2 is much more efficient than the least order hybrid stress elements developed in [Punch and Atluri (1984b)].

It can be seen that the present HMFEM-2 formulation mainly improves the performance of lower order (8-noded) bricks dramatically; however, at a modest increase in computational cost.

4.3.2 Patch test

Consider a standard stress patch test. Cube of side length "L" fixed from one side and is subjected to uniform tensile strength as shown in Figure 6 before. The cube is meshed by 8 brick elements, once in a regular configuration and again in an irregular configuration which is shown in Figure 19. The geometrical properties of this problem is L = 1 and e = L/6 for the irregular mesh, while the material properties are: E = 1 and ν= 0.25.

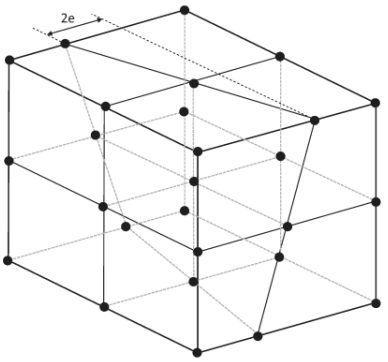

Figure 19: The irregular mesh configurations for the patch test

Table 9 shows the errors for all the elements for the cases of regular and irregular meshes as defined in equation (48). The errors are very small for all the elements and thus, all pass the constant stress patch test.

Considering a displacement patch test, and instead of applying a uniform stress

Table 7: Eigenvalues of the stiffness matrix of the twenty-node brick elements in the original coordinate system

Eigenvalue	Elements				
	DPFEM-B20	HMFEM-2 (B20)		DPFEM-B20	HMFEM-2 (B20)
1	0	0	31	0.4387	0.4335
2	0	0	32	0.4812	0.4335
3	0	0	33	0.4812	0.4335
4	0	0	34	0.6965	0.5975
5	0	0	35	0.6965	0.5975
6	0	0	36	0.6965	0.5975
7	0.0752	0.0585	37	0.7322	0.6988
8	0.0752	0.0585	38	0.7322	0.6988
9	0.0752	0.0585	39	0.8513	0.6988
10	0.0788	0.0877	40	0.8513	0.7322
11	0.0788	0.0877	41	0.8513	0.7322
12	0.0954	0.0877	42	1.2116	0.9006
13	0.0954	0.0883	43	1.2457	1.1665
14	0.0954	0.0883	44	1.2457	1.1665
15	0.1099	0.1099	45	1.2457	1.1665
16	0.1099	0.1099	46	1.268	1.1791
17	0.1422	0.1422	47	1.268	1.1791
18	0.1949	0.1856	48	1.268	1.1791
19	0.1949	0.1856	49	1.6771	1.6398
20	0.1949	0.1856	50	1.6771	1.6398
21	0.2817	0.2931	51	1.6771	1.6398
22	0.288	0.2931	52	2.1623	2.1623
23	0.288	0.2931	53	2.1623	2.1623
24	0.288	0.3509	54	3.4842	2.3885
25	0.289	0.3579	55	3.4842	2.3885
26	0.289	0.3579	56	3.4842	2.3885
27	0.289	0.3592	57	5.4002	5.4002
28	0.3687	0.3592	58	5.5293	5.4953
29	0.4387	0.3592	59	5.5293	5.4953
30	0.4387	0.3687	60	5.5293	5.4953

Table 8: CPU time (in seconds) required for computing the stiffness matrix of each element, normalized to that of the DPFEM elements in the last row

	Element					
CPU	DPFEM-B8	HMFEM-2 (B8)	LO-B8	DPFEM-B20	HMFEM-2 (B20)	LO-B20
Time	0.001772	0.002742	0.0072	0.00985	0.0124	0.0641
	1	1.5474	4.06	1	1.2586	6.5063

Table 9: Performance of different 3D elements in the constant stress patch test

Mesh	DPFEM-B8	HMFEM-2 (B8)	DPFEM-B20	HMFEM-2 (B20)
Regular	9.6061×10^{-16}	1.4932×10^{-16}	3.0132×10^{-15}	3.5245×10^{-15}
Irregular	1.0761×10^{-15}	9.9588×10^{-16}	2.5556×10^{-15}	1.600×10^{-4}

field on the plate, a uniform displacement is applied, and the displacement of the center point of the plate is compared to the exact solution.

Table 10 shows the errors for all the elements for the cases or regular and irregular meshes as defined in equation (49). The errors are very small for all the elements and thus, all pass the uniform displacement patch test.

Table 10: Performance of different 3D elements in the uniform displacement patch test

Mesh	DPFEM-B8	HMFEM-2 (B8)	DPFEM-B20	HMFEM-2 (B20)
Regular	2.4722×10^{-16}	2.2640×10^{-16}	8.7887×10^{-16}	2.9716×10^{-15}
Irregular	4.5280×10^{-16}	3.6835×10^{-16}	5.8252×10^{-16}	2.6719×10^{-6}

4.3.3 Sensitivity to element distortion

In order to test the sensitivity of the elements to mesh distortion, the same problem can be used but this time the cantilever beam is composed of only two distorted elements as shown in Figure 20. The distortion ratio is defined as 2e/L. the geometrical properties for this test is: L = 10, W = 2 and t = 2 while the material properties are: E = 1 and $\nu = 0$. The black dots are the nodes of the 8-node brick elements while the white dots are the nodes to be added for the case of the 20-node elements.

The exact solution of this problem with end bending moment can be found in [Tim-

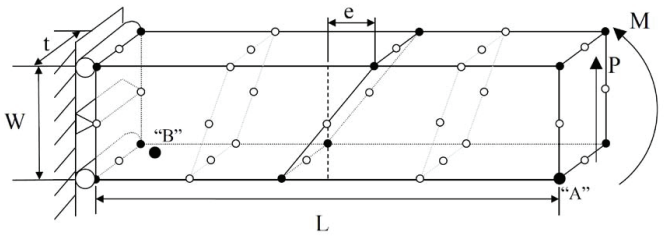

Figure 20: Test of sensitivity to element distortion, cantilever beam under end loading

oshenko and Goodier (1976)] as:

$$
\begin{aligned}
u &= -\frac{\nu xy}{R} \\
v &= \frac{1}{2R}[z^2 + \nu(y^2 - x^2)] \\
w &= -\frac{yz}{R} \\
\sigma_z &= -\frac{Ey}{R} \\
\sigma_x &= \sigma_y = \tau_{xy} = \tau_{yz} = 0
\end{aligned}
\tag{58}
$$

Where:

$$
R = \frac{EI_x}{M} \quad I_x = \frac{tW^3}{12} \tag{59}
$$

z is the longitudinal axis of the beam, y is directed upward, and x is perpendicular on the page.

The exact 2D solution for the end shear case mentioned in equation (50) can also be used here for the 3D case.

Figure 21 shows the effect of varying the distortion ratio on the computed relative stress and the computed relative displacement (FE/Exact) for the eight-node brick elements for the end shear case, while Figure 22 shows that of the end bending case. Figure 23 and Figure 24 show the same plots for the twenty-node brick elements.

These figures show that for both loading conditions the accuracy of HMFEM-2 is always better than that of the DPFEM for the whole range of distortion ratios. However, as the order of the elements is increased, the difference in accuracy between the two types of elements is decreased. This is because the higher order elements generally have high accuracy, hence the superiority of the HMFEM-2 becomes insignificant.

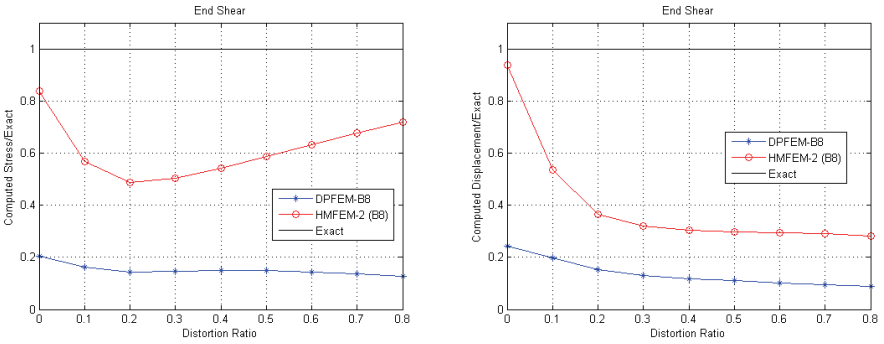

Figure 21: Relative stress at point "B" and relative displacement at point "A" for the 3D 8-noded brick elements for end shear load case

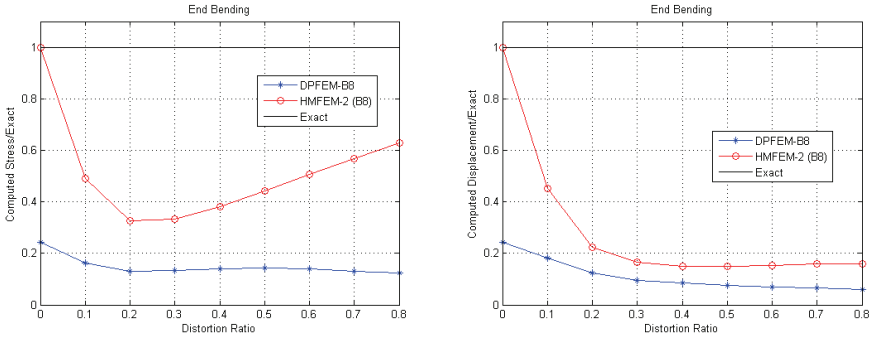

Figure 22: Relative stress at point "B" and relative displacement at point "A" for the 3D 8-noded brick elements for end bending load case

5 Three-Dimensional Voronoi cell finite element

5.1 3D VCFEM-RBF-W formulation

For an arbitrary polyhedron (3D Voronoi cell) element in the 3D space as in Figure 25 with n nodes $\mathbf{x}^1$, $\mathbf{x}^2$, ... $\mathbf{x}^n$, with corresponding nodal displacements u_i^1, u_i^2, ... u_i^{n}, a smooth linear displacement field assumption on each surface can be used:

$$u_i^S = \sum_{k=1}^{n} N^{*k}(\mathbf{x})\, u_i^k \quad \text{at } \partial\Omega_m \tag{60}$$

Dealing with polygonal surfaces, Barycentric coordinates should be used to de-

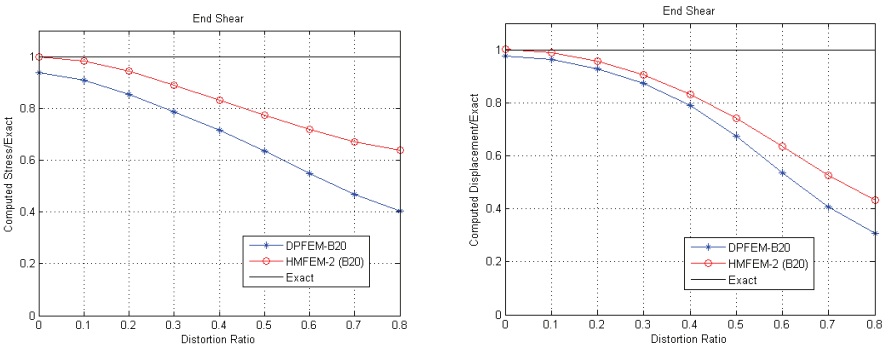

Figure 23: Relative stress at point "B" and relative displacement at point "A" for the 3D 20-noded brick elements for end shear load case

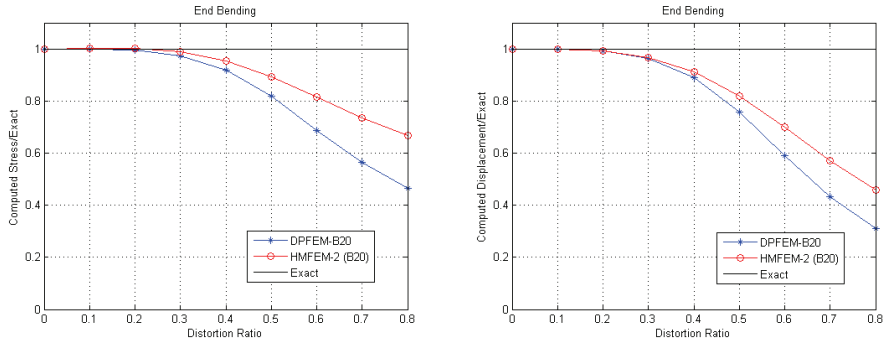

Figure 24: Relative stress at point "B" and relative displacement at point "A" for the 3D 20-noded brick elements for end bending load case

scribe the displacement field. The Barycentric coordinates, denoted as $\lambda_i (i = 1, 2, \ldots m)$ where m is the number of the vertices of the convex polygon, in general should satisfy two properties:

1. Non-negative: $\lambda_i \geq 0$ on Ω_m.
2. Linear completeness: For any linear function $f(\mathbf{x}) : \Omega_m \rightarrow \mathrm{R}$,

   $f(\mathbf{x}) = \sum_{i=1}^{m} f(\mathbf{x^i})\lambda_i$

   Any set of Barycentric coordinates under this definition also satisfies:

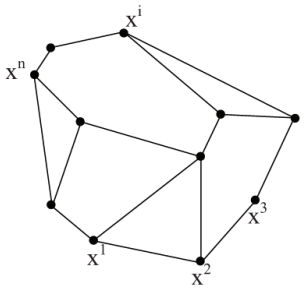

Figure 25: Polyhedron (3D Voronoi cell) element with arbitrary number of polygonal faces

3. Partition of unity: $\sum_{i=1}^{n} \lambda_i \equiv 1$.
4. Linear precision: $\sum_{i=1}^{n} \mathbf{x^i} \lambda_i(x) = \mathbf{x}$.
5. Dirac delta: $\lambda_i(\mathbf{x^j}) = \delta_{ij}$.

In this paper, we use the Wachspress coordinates [Wachspress (1975)], defined as follows:

Let $\mathbf{x} \in \Omega$, and define the areas: B_i as the area of the triangle having $\mathbf{x^{i-1}}, \mathbf{x^i}$ and $\mathbf{x^{i+1}}$ as its three vertices, and $A_i(\mathbf{x})$ as the area of the triangle having $\mathbf{x}$, $\mathbf{x^i}$ and $\mathbf{x^{i+1}}$ as its three vertices. This is illustrated in Figure 26.

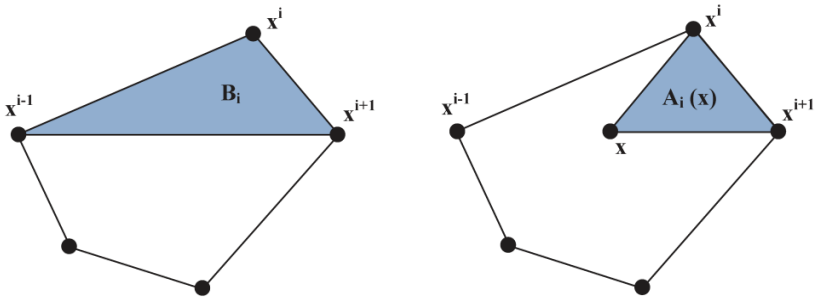

Figure 26: Definition of triangles B_i and $A_i(\mathbf{x})$

Define the Wachspress weight function as:

$$w_i(\mathbf{x}) = B_i \prod_{j \neq i, i-1} A_j(\mathbf{x}) \tag{61}$$

Then, the Wachspress coordinates are given by the rational functions:

$$\lambda_i(\mathbf{x}) = \frac{w_i(\mathbf{x})}{\sum_{j=1}^{m} w_j(\mathbf{x})} \tag{62}$$

Similar to the well-known triangular coordinates used in the 2D triangular elements, where the shape functions associated with the three vertices are indeed the triangular coordinates themselves, the shape functions associated with the vertices of this polygonal surface displacement field are the Barycentric coordinates. The triangular coordinates are actually a special case of the Barycentric coordinates when the polygon is just a triangle.

So, equation (60) becomes:

$$u_i^S = \sum_{k=1}^{n} \lambda_i^k(\mathbf{x})\, u_i^k \quad \text{on } \partial\Omega_m \quad \text{or} \quad \mathbf{u}^S = \mathbf{N}^*(\mathbf{x})\mathbf{q} \tag{63}$$

Inside the element, an interior displacement field, as compactly-supported radial basis functions (CS-RBF), is assumed. The CS-RBF has the advantages of positive definetness, Dirac delta property and relatively simple forms of spatial derivatives. The CS-RBF have been widely used recently by [Wu (1995); Atluri, Han, and Rajendran (2004), for example]. The lack of their completeness has been overcome by introducing additional polynomial functions as in [Golberg, Chen, and Bowman (1999)]. Under such an assumption, the interior displacement field is represented as:

$$u_i^I = \mathbf{R}^{\mathbf{T}}(\mathbf{x})\mathbf{a} + \mathbf{P}^{\mathbf{T}}(\mathbf{x})\mathbf{b} \quad \text{in } \Omega_m \tag{64}$$

Where $\mathbf{R}^{\mathbf{T}}(\mathbf{x}) = [R^{r1}(\mathbf{x}) \;\; R^{r2}(\mathbf{x}) \ldots R^{rl}(\mathbf{x})]$ is a set of radial basis functions centered at l points $\mathbf{x}^{r1}$, $\mathbf{x}^{r2}$, ... $\mathbf{x}^{rl}$ on $\partial\Omega_m$; $\mathbf{P}^{\mathbf{T}}(\mathbf{x}) = [P^1(\mathbf{x}) \;\; P^2(\mathbf{x}) \ldots P^m(\mathbf{x})]$ is a set of m monomial functions which are complete to a certain order; $\mathbf{a}$, $\mathbf{b}$ are coefficient vectors.

Equation (64) can be written as:

$$\mathbf{u}^I = \mathbf{M}(\mathbf{x})\boldsymbol{\alpha} \quad \text{in } \Omega_m \tag{65}$$

Where $\mathbf{M}(\mathbf{x}) = \begin{bmatrix}\mathbf{R}^{\mathbf{T}}(\mathbf{x}) & \mathbf{P}^{\mathbf{T}}(\mathbf{x})\end{bmatrix}$ and $\boldsymbol{\alpha} = \begin{Bmatrix}\mathbf{a}\\ \mathbf{b}\end{Bmatrix}$.

While various radial basis functions can be used, in the current study, we use:

$$R^{rl}(\mathbf{x}) = \begin{cases} \left(1 - \frac{d^{rl}(\mathbf{x})}{r^{rl}}\right)^3 \left(1 + 3\frac{d^{rl}(\mathbf{x})}{r^{rl}}\right) & d^{rl}(\mathbf{x}) < r^{rl} \\ 0 & d^{rl}(\mathbf{x}) \geq r^{rl} \end{cases} \tag{66}$$

Where $d^{rl}(\mathbf{x}) = \left|\mathbf{x} - \mathbf{x}^{rl}\right|$ is the Euclidean distance from point $\mathbf{x}$ to point $\mathbf{x}^{rl}$, and r^{rl} is the support size of $R^{rl}(\mathbf{x})$.

In this study, a first order complete polynomial basis is used:

$$\mathbf{P^T}(\mathbf{x}) = \begin{bmatrix} 1 & x & y & z \end{bmatrix} \tag{67}$$

The compatibility between the surface displacements of the element, as in equation (63) and the interior displacement field, as in equation (64) or (65), at the surface $\partial\Omega_m$, can be enforced in many ways, including:

(a) The method of minimizing boundary-least-squares error between u_i^S and u_i^I at $\partial\Omega_m$, or

(b) The boundary collocation between u_i^S and u_i^I at selected points on $\partial\Omega_m$.

Both methods are presented in the following:

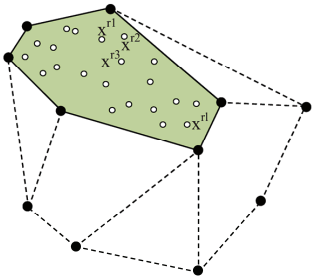

Figure 27: Collocation points on the boundary surfaces of the 3D VCFEM-RBF-W

Using the Collocation method:

The coefficients are obtained by enforcing the compatibility condition of the interior and the surface displacements at collocation points $\begin{bmatrix}\mathbf{x}^{r1}, & \mathbf{x}^{r2}, & \ldots & \mathbf{x}^{rl}\end{bmatrix}$(see Figure 27) which leads to:

$$\begin{bmatrix} \mathbf{R}_0 & \mathbf{P}_0 \\ \mathbf{P}_0^T & \mathbf{0} \end{bmatrix} \begin{Bmatrix} \mathbf{a} \\ \mathbf{b} \end{Bmatrix} = \begin{Bmatrix} \mathbf{u}_i^r \\ \mathbf{0} \end{Bmatrix} \tag{68}$$

$$\mathbf{R}_0 = \begin{bmatrix} R^{r1}(\mathbf{x}^{r1}) & R^{r2}(\mathbf{x}^{r1}) & \ldots & R^{rl}(\mathbf{x}^{rl}) \\ R^{r1}(\mathbf{x}^{r2}) & R^{r2}(\mathbf{x}^{r2}) & \ldots & R^{rl}(\mathbf{x}^{r2}) \\ \vdots & \vdots & \vdots & \vdots \\ R^{r1}(\mathbf{x}^{rl}) & R^{r2}(\mathbf{x}^{rl}) & \ldots & R^{rl}(\mathbf{x}^{rl}) \end{bmatrix} \tag{69}$$

$$\mathbf{P}_0 = \begin{bmatrix} P^1(\mathbf{x}^{r1}) & P^2(\mathbf{x}^{r1}) & \dots & P^l(\mathbf{x}^{rl}) \\ P^1(\mathbf{x}^{r2}) & P^2(\mathbf{x}^{r2}) & \dots & P^l(\mathbf{x}^{r2}) \\ \vdots & \vdots & \vdots & \vdots \\ P^1(\mathbf{x}^{rl}) & P^2(\mathbf{x}^{rl}) & \dots & P^l(\mathbf{x}^{rl}) \end{bmatrix} \tag{70}$$

$$\begin{aligned} \mathbf{u}_i^{rT} &= \begin{bmatrix} u_i^{r1} & u_i^{r2} & \dots & u_i^{rl} \end{bmatrix} \\ &= \begin{bmatrix} \sum_{k=1}^{n} N^{*k}(\mathbf{x}^{r1}) u_i^k & \sum_{k=1}^{n} N^{*k}(\mathbf{x}^{r2}) u_i^k & \dots & \sum_{k=1}^{n} N^{*k}(\mathbf{x}^{rl}) u_i^k \end{bmatrix} \end{aligned} \tag{71}$$

Solving equation (68) gives:

$$\mathbf{a} = \mathbf{G_r}\mathbf{u}_i^r \quad \text{and} \quad \mathbf{b} = \mathbf{G_p}\mathbf{u}_i^r \tag{72}$$

So the interior displacement field has the form:

$$u_i^I = \left[\mathbf{R^T}(\mathbf{x})\mathbf{G_r} + \mathbf{P^T}(\mathbf{x})\mathbf{G_p}\right]\mathbf{u}_i^r = \sum_{k=1}^{n} N^k(\mathbf{x}) u_i^k \quad \text{in } \Omega_m \tag{73}$$

In terms of nodal displacement vector $\mathbf{q}$, the interior displacement field are expressed as:

$$\mathbf{u}^I = \mathbf{N}(\mathbf{x})\mathbf{q} \quad \text{in } \Omega_m \tag{74}$$

The corresponding interior strains are:

$$\mathbf{u}_{(i,j)}^I = \mathbf{B}(\mathbf{x})\mathbf{q} \quad \text{in } \Omega_m \tag{75}$$

Now, we can use the principle of minimum potential energy (16) to obtain the finite element equation for any of the two mentioned methods:

$$\begin{aligned} &\delta\pi(\mathbf{q}) = 0 \\ &\delta\pi(\mathbf{q}) = \delta \sum_m \left\{ \int_{\Omega_m} \left[\tfrac{1}{2}\mathbf{q}^T \mathbf{B}^T(\mathbf{x})\mathbf{D}\mathbf{B}(\mathbf{x})\mathbf{q} - \mathbf{q}^T \mathbf{N}^T(\mathbf{x})\bar{\mathbf{f}} \right] d\Omega - \int_{S_{tm}} \mathbf{q}^T \mathbf{N}^{*T}(\mathbf{x})\bar{\mathbf{t}} dS \right\} \\ &\delta\pi(\mathbf{q}) = \sum_m \left[\delta\mathbf{q}^T \int_{\Omega_m} \mathbf{B}^T(\mathbf{x})\mathbf{D}\mathbf{B}(\mathbf{x}) d\Omega \mathbf{q} - \delta\mathbf{q}^T \left(\int_{\Omega_m} \mathbf{N}^T(\mathbf{x})\bar{\mathbf{f}} d\Omega + \int_{S_{tm}} \mathbf{N}^{*T}(\mathbf{x})\bar{\mathbf{t}} dS \right) \right] \\ &\delta\pi(\mathbf{q}) = \sum_m \left(\delta\mathbf{q}^T \mathbf{K}^e \mathbf{q} - \delta\mathbf{q}^T \mathbf{Q} \right) \end{aligned} \tag{76}$$

Where $\mathbf{K}^e$ and $\mathbf{Q}$ are defined as:

$$\mathbf{K}^e = \int_{\Omega_m} \mathbf{B}^T(\xi^\gamma)\mathbf{D}\mathbf{B}(\xi^\gamma) d\Omega \tag{77}$$

and

$$\mathbf{Q} = \int_{\Omega_m} \mathbf{N}^T(\xi^\gamma)\bar{\mathbf{f}}d\Omega + \int_{S_{tm}} \mathbf{N}^{*T}(\xi^\gamma)\bar{\mathbf{t}}dS \tag{78}$$

[Dong and Atluri (2011a)] proved that for the VCFEM-RBF to pass the patch test, when the collocation method is used, with an error reduced to a satisfactory level, the interior and boundary displacements should be collocated at the quadrature points. So, for VCFEM-RBF-W, the collocation points are the 2D triangular quadrature points on the triangles generated by triangulating each polygonal surface.

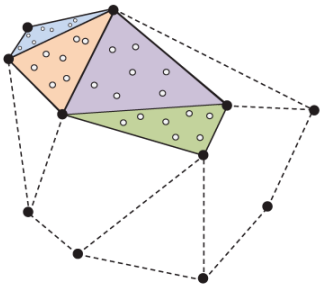

Figure 28: Collocation points on one surface of VCFEM-RBF-W

In principle, as the number of quadrature points increases, the error in the patch test is decreased provided that a sufficient quadrature order is used in the integration of the stiffness matrix. However, since the integrands in the stiffness matrix are not polynomials, the numerical quadrature always gives an approximate solution whatever the order of the quadrature. Three-dimensional Delaunay triangulation is used to divide each Voronoi cell finite element into a number of tetrahedrons in order to use the 3D tetrahedron numerical quadrature in calculating the stiffness matrix of each element. In this work, we use 7 2D triangular quadrature points, on each of the triangles generated by triangulating each polygonal surface, as the collocation points (See Figure 28) for enforcing the boundary-displacement compatibility. We use 11 or 15 quadrature points in each tetrahedron, for integrating the stiffness matrix in order to obtain sufficiently accurate results.

It should be mentioned here that the matrix that is being inverted in equation (68), in order to obtain $\mathbf{a}$ and $\mathbf{b}$, has dimensions $n \times n$, where n is the number of RBF basis functions plus the number of the P basis functions. Here, the number of RBF basis functions is taken to be exactly the number of collocation points, and the RBF centers are taken to be exactly the collocation points in the whole element. Thus,

n = number of collocation points + 4, which is n= 7× number of triangles on all boundaries + 4 in our case.

Using the Least squares method:

When the number of collocation points is increased to a limit of infinity, it is equivalent to enforcing the compatibility between $\mathbf{u}^I$ and $\mathbf{u}^S$ using the least squares method, namely minimizing the following functional:

$$\begin{aligned} e(\boldsymbol{\alpha},\mathbf{q}) &= \int_{\partial\Omega_m} (u_i^I - u_i^S)(u_i^I - u_i^S)\, dS \\ &= \int_{\partial\Omega_m} (\boldsymbol{\alpha}^T\mathbf{M}^T\mathbf{M}\boldsymbol{\alpha} - 2\boldsymbol{\alpha}^T\mathbf{M}^T\mathbf{N}^*\mathbf{q} + \mathbf{q}^T\mathbf{N}^{*T}\mathbf{N}^*\mathbf{q})\, dS \\ &= \boldsymbol{\alpha}^T\mathbf{U}\boldsymbol{\alpha} - 2\boldsymbol{\alpha}^T\mathbf{V}\mathbf{q} + \mathbf{q}^T\mathbf{W}\mathbf{q} \end{aligned} \tag{79}$$

Where equations (63) and (65) are used.

To minimize e for a fixed $\mathbf{q}$, we have,

$$\delta e(\delta\boldsymbol{\alpha},\mathbf{q}) = 2\delta\boldsymbol{\alpha}^T\mathbf{U}\boldsymbol{\alpha} - 2\delta\boldsymbol{\alpha}^T\mathbf{V}\mathbf{q} = 0 \tag{80}$$

This should be true for any $\delta\boldsymbol{\alpha}$, hence;

$$\mathbf{U}\boldsymbol{\alpha} = \mathbf{V}\mathbf{q} \quad \text{or} \quad \boldsymbol{\alpha} = \mathbf{U}^{-1}\mathbf{V}\mathbf{q} = \mathbf{L}\mathbf{q} \tag{81}$$

Substituting this into equation (65) gives:

$$\mathbf{u}^I = \mathbf{M}(\mathbf{x})\boldsymbol{\alpha} = \mathbf{M}(\mathbf{x})\mathbf{L}\mathbf{q} = \mathbf{N}(\mathbf{x})\mathbf{q} \quad \text{in } \Omega_m \tag{82}$$

Hence, the strain field can be determined as in equation (75), and the principle of minimum potential energy can be used as done in equation (76) in order to get the stiffness matrix $\mathbf{K}^e$ and the load vector $\mathbf{Q}$ as in equation (78).

Only the square matrix $\mathbf{U} = \int_{\partial\Omega_m} \mathbf{M}^T\mathbf{M}\, dS$ is being inverted here. The dimensions of this matrix is also $n\times n$ where n is the number of RBF basis functions plus the number of the P basis functions. If we take the number of RBF basis to be exactly the same as that of the integration points in the whole element as we did in the case of the collocation method, the number of unknowns $\boldsymbol{\alpha} = \begin{bmatrix}\mathbf{a} & \mathbf{b}\end{bmatrix}^T$ will be larger than that of the equations (in a collocation sense) by the number of the P-basis functions (4 here). So the number of integration points in the whole element used in evaluating $\mathbf{U}$ and $\mathbf{V}$ matrices should be larger than that of the RBF basis functions.

Here, we selected the RBF centers to be at the 3 Gaussian points in each triangle of the triangulated boundary surfaces, while 7 Gaussian points per triangle are used

in integration. Hence the number of RBF basis functions is $3\times$ number of triangles on all boundaries. This number of RBF basis functions proved to be enough to give sufficient accuracy of the element unlike the case of the collocation method where 7 collocation points per triangle are required to give an acceptable accuracy. Thus, $n= 3\times$ number of triangles on all boundaries + 4. This number n is much less than that used in the collocation method and hence the least square method yields a much cheaper element while also leading to a better accuracy as will be illustrated in the numerical examples in the following section.

Comparing the features of the formulation of VCFEM-RBF-W with that of [Ghosh and Moorthy (2004)], the only available 3D VCFEM model in the literature, we note the superiority of this new formulation in the following:

1. VCFEM-RBF-W is based on displacement fields only and the use of the principle of minimum potential energy, thus the present formulation avoids the LBB conditions. Ghosh's formulation, on the other hand, is based on assuming both an inter-element compatible boundary-displacement field, and an "a priori equilibrated" stress field inside the element, and the use of a multi-field functional in the modified principle of minimum complementary energy, thus it contains Lagrangian multipliers and is plagued with the LBB conditions (which are impossible to be satisfied a priori).

2. The use of hybrid stress formulation involves the generation of two additional element matrices (**H** and **G**), through quadrature over each element, in constructing the element stiffness matrix; **H** should be inverted, thus raising the computational cost, and the rank of **G** (3 times the number of nodes in the 3-D VCFEM, less 6, the number of rigid modes for each element) should be assured a priori.

3. The use of hybrid stress formulation, which requires an equilibrated stress field, involves the assumption of six stress functions. However, Ghosh's formulation used Maxwell or Morera's simplifications to reduce the number of stress functions to three. Maxwell and Morera's simplifications produce stress fields that are not always complete.

4. VCFEM-RBF-W uses Wachspress functions as the boundary surface displacements, and hence avoids adding additional nodes inside the surfaces. However, Ghosh's formulation divides each surface of the VCFEM into triangles, after adding a center node in each surface.

5. VCFEM-RBF-W formulation is much simpler, and computationally more efficient.

Extending the modeling of VCFEM-RBF-W to include the presence of voids and inclusions will be presented in a future work.

5.2 Numerical Examples and Applications

In order to test the performance of the new element, some numerical tests will be illustrated here. The properties that will be tested are: Stiffness, Invariance, stability, and patch test. The element will then be used to model a representative volume element (RVE) of a functionally graded material (FGM) with different volume fractions of the two constituents in a tension test to determine the effective elastic material properties.

5.2.1 Stiffness, Invariance and Stability

A single cube element is considered here, with its 8 corners having Cartesian coordinates: (-1,-1,-1), (1,-1,-1), (1,1,-1), (-1,1,-1), (-1,-1,1), (1,-1,1), (1,1,1), (-1,1,1). The material properties are: E = 1, and ν = 0.25. The eigenvalues of the element in Cartesian coordinates are computed to compare the stiffness of the three-dimensional element VCFEM-RBF-W, using both the mentioned displacement compatibility enforcing methods, with the primal displacement-based finite element (DPFEM) and the Hybrid/Mixed element HMFEM-2 discussed before. Then the global Cartesian coordinate system is rotated counterclockwise by any arbitrary angle θ once around the x-axis, then around y-axis and again around z-axis. After each rotation, the eigenvalues are computed in order to check the invariance property.

Table 11 shows the eigenvalues of the different 3D elements. It can be seen that, first, all the elements are stable because only six zero eigenvalues exist for each element corresponding to the six rigid-body modes. Second, the lower eigenvalues of the new VCFEM-RBF-W element (using collocation method) are larger than that of the HMFEM-2 (B8) element which means that the VCFEM-RBF-W element is stiffer, but the eigenvalues of the VCFEM-RBF-W element (using collocation method) are comparable with the DPFEM-B8 element, which means similar stiffness. The VCFEM-RBF-W element using the least squares method is stiffer than the element developed by using the collocation method.

Exactly the same eigenvalues were obtained when the original coordinate system is rotated around any coordinate axis by any angle. Thus, the new VCFEM-RBF-W element proves to be invariant whatever the shape or the distortion of the element.

It should be mentioned that in evaluating the eigenvalues of the VCFEM-RBF-W, with rotation of the coordinate axis, the same tetrahedrons connectivity should be used in integrating the element stiffness matrix in order to get the same eigenvalues.

Table 11: Eigenvalues of the stiffness matrix of a cube using different elements

Eigenvalue	Elements			
	DPFEM-B8	HMFEM-2 (B8)	VCFEM-RBF-W (Collocation)	VCFEM-RBF-W (Least squares)
1	0	0	0	0
2	0	0	0	0
3	0	0	0	0
4	0	0	0	0
5	0	0	0	0
6	0	0	0	0
7	0.1333	0.1333	0.1378	0.1898
8	0.1333	0.1333	0.1382	0.1936
9	0.2222	0.1333	0.2429	0.2443
10	0.2222	0.1333	0.2454	0.2732
11	0.2222	0.1333	0.2475	0.2899
12	0.4	0.2667	0.4067	0.4581
13	0.4	0.2667	0.4135	0.4666
14	0.4	0.2667	0.4155	0.5031
15	0.5333	0.5333	0.5484	0.6180
16	0.6667	0.5333	0.6828	0.7586
17	0.6667	0.5333	0.6830	0.7736
18	0.6667	0.5333	0.6914	0.7927
19	0.8	0.8	0.8	0.8
20	0.8	0.8	0.8	0.8
21	0.8	0.8	0.8	0.8
22	0.8	0.8	0.8	0.8
23	0.8	0.8	0.8	0.8
24	2	2	2	2

This is because the integrands of the stiffness matrix contain radial basis functions (RBF) which are not polynomials and hence any numerical quadrature will give approximate solutions not exact ones. So, the eigenvalues of the element stiffness matrix will be slightly different if we change the way of domain decomposition. Also, the same quadrature order should be used for all cases in integrating the stiffness matrix, since as per the previous reason, the stiffness matrix will slightly change as the order of integration changes.

5.2.2 Patch test

First, a single cube element similar to that of the previous section with the same material properties is tested in a constant stress patch test and the result is compared with the analytical solution. Then a cubic domain of side length equal to 10 is meshed using 10 arbitrary 3D Voronoi cell finite elements, as shown in Figure 29, and tested under the same constant stress patch test.

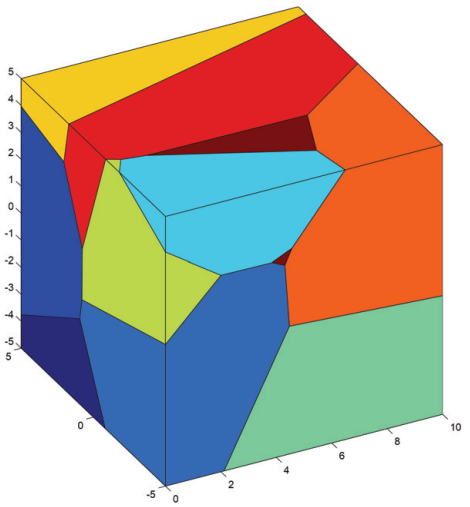

Figure 29: Domain meshed using 10 Voronoi cell finite elements The

The error in all the nodal displacements, defined in equation (48) is tabulated in Table 12 for the two tests for VCFEM-RBF-W using the collocation and the least squares methods.

The mesh configuration in Figure 29 is also used in the uniform displacement patch test, and the error of all the nodal displacements (Not only the center node), defined in equation (48), is also calculated and tabulated in Table 12.

As can be seen from Table 12, even though the Least squares method gives less error than that of the collocation method for the case of single cube element in the patch test, as the domain is meshed using multi elements, the performance of both methods is similar. However, the least squares method is much cheaper as mentioned earlier and hence it is recommended to be used in the 3D VCFEM-RBF-W. This is unlike the case of the 2D VCFEM in [Dong and Atluri (2011b); Dong and Atluri (2012)] where it was shown that the collocation method is the least computationally intensive and the most accurate method for enforcing displacement compatibility.

Table 12: Eigenvalues of the stiffness matrix of a cube using different elements

Test		VCFEM-RBF-W (Collocation)	VCFEM-RBF-W (Least squares)
Constant stress patch test	single cube	8.7×10^{-3}	3.9×10^{-3}
	Domain of 10 arbitrary VCFEM	6.0×10^{-3}	6.1×10^{-3}
Uniform displacement patch test	Domain of 10 arbitrary VCFEM	5.7×10^{-3}	5.8×10^{-3}

It should be mentioned that, as the mesh configuration of the domain changes, the error in the patch tests will slightly change, since the numerical integration of the stiffness matrices of the elements is always approximate and never reach the exact solutions. Different mesh configurations were tested in patch tests of different domains and the error never exceeds the 1%. Thus, the new VCFEM-RBF-W element can pass the patch tests with satisfactorily small error.

5.2.3 FGM effective material properties determination

One of the most important applications, that this new 3D Voronoi cell finite element can be used for, is the determination of the effective properties of functionally graded materials (FGM). These materials have microstructure and properties that vary in a continuous fashion, from one material to the other. The use of these materials reduces the service stresses of ceramic-coated metallic parts and the stresses developed during fabrication due to the differences in thermo-mechanical properties of metals and ceramics. Thus, replacing the sharp ceramic/material interface with an intermediate graded layer of FGM can stop problems like decohesion at the ceramic/metal interface, plastic deformation and void nucleation in metal, and cracking within the ceramic. A schematic of a FGM is shown in Figure 30 to illustrate how the microstructure varies in a complex fashion from one pure material to the other.

It is important to study the distribution of stresses and the stress reduction mechanisms in these functionally graded materials, as well as determining the effective material properties of these heterogeneous materials as a function of the volume fractions of the constituent materials.

Several models have been developed to predict the effective elastic properties of heterogeneous materials and their dependence on materials microstructure.

Based on the Eshelby's equivalent inclusion method [Eshelby (1957)], a number

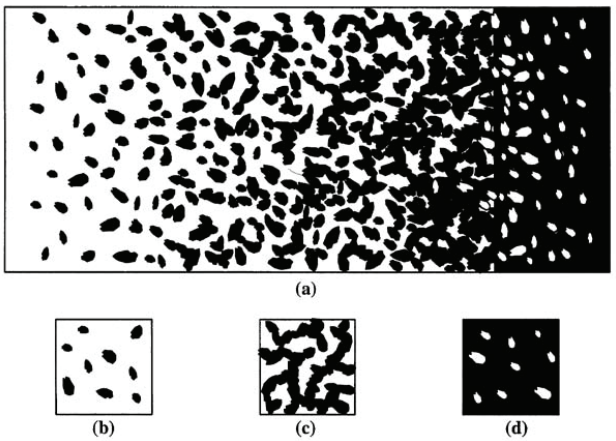

Figure 30: (a) A schematic representation of the variation in FGM microstructure: (b) and (d) typical microstructure at small volume fractions of the two materials; (c) typical microstructure at comparable volume fractions of the two materials

of self-consistent models were proposed [Hill (1965); Budiansky (1965); Hori and Nemat-Nasser (1993)]. These models are generally successful in predicting the effective material properties only for relatively simple microstructures and low volume fractions of the inclusions.

Based on the finite element analysis, a number of models that overcome the limitation of the low volume fraction of the inclusion were proposed [Christman, Needleman, and Suresh (1989); Tvergaard (1990); Bao, Hutchinson, and McMeeking (1991)]. These models assume that the heterogeneous material can be represented as a periodic repetition of a representative material element (RME). However, the real microstructures are rarely periodic. Consequently, non-homogeneity and nonlinearity in deformation at the structure length scale, which may occur under complex loading conditions, may not be predicted, if this local periodicity constraint is imposed.

[Grujicic and Zhang (1998)] used the two dimensional Voronoi cell finite element to determine the effective elastic properties of FGM. They used the 2D VCFEM developed by Ghosh and co-workers in a series of papers [Ghosh and Mukhopadhyay (1991); Ghosh and Mallett (1994); Ghosh, Lee, and Moorthy (1995)].

Following [Grujicic and Zhang (1998)], the microstructure of the FGM can be modeled as a 3D Voronoi cell finite elements with embedded inclusions if the volume fraction (VF) of any of the two constituent materials ranges from 0 to 0.3, and as some intertwined clusters of the two phases if the VF of any of the materials ranges

from 0.4 to 0.6. In the regions where the VF of one constituent ranges from 0.3 to 0.4, the microstructure is treated as consisting of the two basic microstructures mentioned above mixed in different proportions.

In order to obtain realistic predictions of a new materials macroscopic behavior by the computational means, three-dimensional numerical simulations of statistically representative micro-heterogeneous material samples are unavoidable.

Extending the 3D Voronoi cell finite element to include 3D inclusions and voids is a nontrivial enterprise, and will be addressed in a future article. For now, we can examine our new VCFEM-RBF-W element (using the least square method) in modeling FGM when the range of the volume fraction of any of the two constituent materials is in the range of 0.4 to 0.6.

Analysis of Ni_3Al/TiC system

Ni_3Al/TiC functionally graded material is considered here. The material properties are as follows: E_{Ni_3Al}= 217 GPa, ν_{Ni_3Al}= 0.30, E_{TiC}= 440 GPa, and ν_{TiC}= 0.19.

In order to account for the randomness of the microstructure, three samples of the RVE are considered in this analysis. Each sample has a different mesh configuration composed of 50 three-dimensional Voronoi cell finite elements. For each mesh configuration, six random distributions of the 2 materials are tested. Data points are calculated for the cases when the volume fraction of Ni_3Al ranges from 0.4 to 0.6.

Figure 31 shows the 3 considered mesh configurations, for different random material distributions for 3 cases with the Ni_3Al volume fraction $\approx$ 0.4, 0.5 and 0.6. In this figure the blue color denotes Ni_3Al while the red color denotes TiC.

The results of the variation of the effective Elasticity modulus (Young's modulus) and the effective Poisson's ratio as the volume fraction of TiC is changed from 0.4 to 0.6 are shown in Figure 32 and compared with the experimental results [Zhai, Jiang, and Zhang (1993)] and other methods from the literature: the self-consistent method (SCM), the Equivalent inclusion method (EIM), and the VCFEM-2D (using 600 elements) [Grujicic and Zhang (1998)].

It is clear from Figure 32 (upper) that the current model gives much better results for the effective Young's modulus than the 2D VCFEM based on Hybrid stress formulation, even though the 3D model used only 50 elements while the 2D used 600. As for the Poisson's ratio variation shown in Figure 32 (lower), the results of the current model are comparable to the other models. Increasing the number of elements in the RVE is expected to increase the resolution of the results. Including the effect of voids is expected to yield more realistic models, and including the presence of inclusions in the VCFEM-RBF-W element is expected to aid in extending the results to all the range of volume fractions.

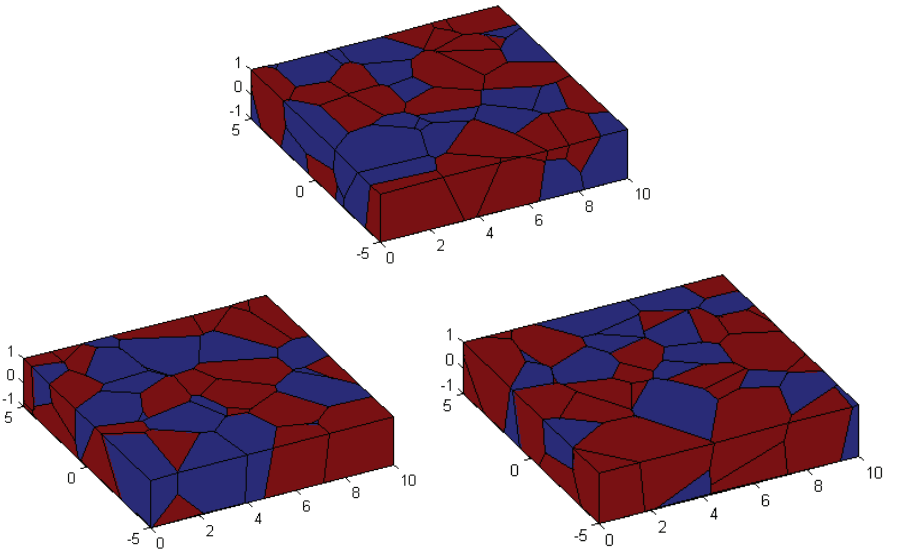

Figure 31: The 3 considered mesh configurations: the first with VF of $Ni_3Al \approx 0.6$, the second with VF of $Ni_3Al \approx 0.5$, the third with VF of $Ni_3Al \approx 0.4$ (The blue color denotes Ni_3Al and the red color denotes TiC)

6 Conclusions

In this paper, the Hybrid/Mixed finite elements based on assumed independent strains and displacements (HMFEM-2 family of elements) is extended to the higher order two-dimensional case (8-node and 9-node quadrilateral elements), and low as well as high-order three-dimensional cases (8-node and 20-node brick elements). This new family of Hybrid/Mixed finite elements, that is not based on multi-field variational principles, proved to be stable, invariant (through the introduction of the element-fixed local orthogonal base vectors of the strain tensor) and less sensitive to mesh distortion compared to the displacement-based elements. The elements can also pass the patch test, avoid the locking phenomenon associated with the well-known primal displacement-based finite elements (DPFEM) and give more accurate results for the computed stresses and strains. This accuracy is much more significant in the lower order cases (4-node quadrilateral elements in 2D and 8-node brick elements in 3D) than in the higher order ones. As the order of the elements is increased, the DPFEM gives high enough accuracy that the difference between the two element types is not highly significant (this is the limitation principle). Because the newly developed elements use the strains derived from the displacement

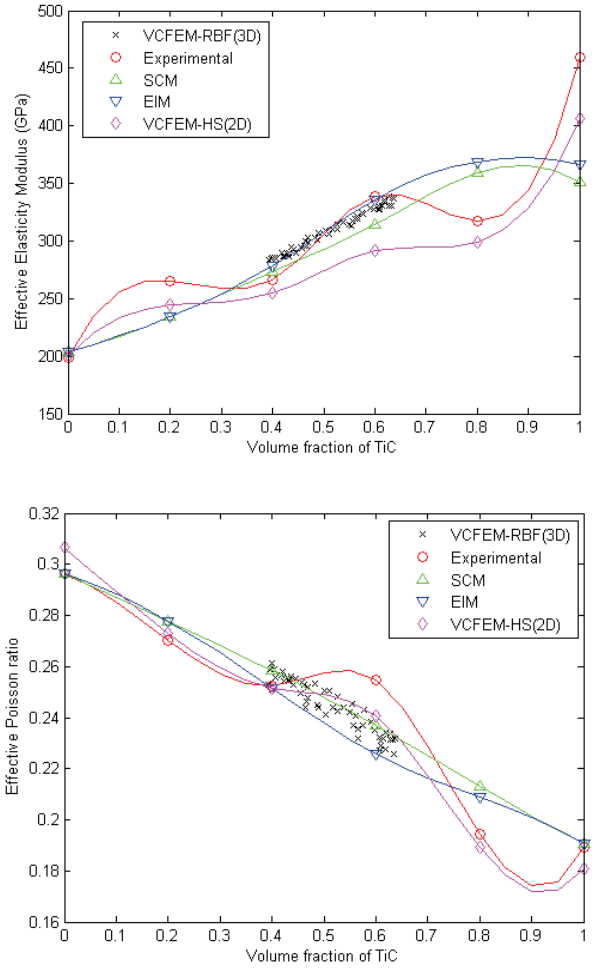

Figure 32: The results of the current model for the Effective Young's modulus (upper) and effective Poisson's ratio (lower) compared to the experimental and other models from the literature

field in order to collocate the strains with the independent strain field, and because of the transformations involved between the coordinate systems, the HMFEM-2 is less computationally efficient than the DPFEM.

However, the HMFEM-2 family is much more efficient than any other hybrid/mixed finite elements developed in the literature such as the least order hybrid stress finite elements [Pian (1964); Punch and Atluri (1984b)].

In this paper also, three-dimensional Voronoi cell finite element (VCFEM) based on radial basis functions (RBF) and Wachspress coordinates is developed. This 3D element, denoted as "VCFEM-RBF-W", proved to be stable, invariant and able to pass the patch tests. The VCFEM-RBF-W is computationally very simple; and at the same time, computationally very efficient, as compared to the hybrid-stress Voronoi cell FEM developed by Ghosh and his colleagues [Ghosh and Mukhopadhyay (1991); Ghosh and Mallett (1994); Ghosh and Moorthy (2004)]. Enforcing the displacement compatibility between the two displacement fields using the least square method yields a much cheaper element than that using the collocation method.

The newly developed VCFEM-RBF-W is used in an important micromechanical application of determining the effective elastic material properties for functionally graded materials. For the considered range of volume fraction variations, the accuracy of the results of this new 3D VCFEM-RBF-W for predicting the variation of the effective Young's modulus as a function of the volume fraction of one of the FGM constituents is better than that of the 2D hybrid stress VCFEM-HS model of [Ghosh and Mallett (1994)] and other methods in the literature, however it gives comparable results for predicting the variation of Poisson's ratio. The resolution is expected to increase as the number of elements is increased. Including voids and inclusions in modeling the VCFEM will be considered in future work and is expected to help in extending the results to the full range of volume fractions and predicting the behavior of FGM in different applications.

Acknowledgement: This work was supported in part by the Vehicle Technology Division of the Army Research Labs, under a collaborative research agreement with University of California, Irvine (UCI), and in part by the Word Class University (WCU) program through the National Research Foundation of Korea, funded by the Ministry of Education, Science and Technology (Grant no.: R33-10049).

References

Atluri, S. N. (1975): On hybrid finite element models in solid mechanics. Vichnevetsky, R. (ed.): *Advances in Computer Methods for Partial Differential Equations*, Proceedings of the international symposium, pp. 346–356. International Organization, AICA.

Atluri, S. N.; Han, Z. D.; Rajendran, A. M. (2004): A new implementation of the meshless finite volume method, through the MLPG "mixed" approach. *CMES: Computer Modeling in Engineering & Sciences*, vol. 6, no. 6, pp. 491–514.

Atluri, S. N.; Tong, P.; Murakawa, H. (1983): Recent studies in hybrid and mixed

finite element methods in mechanics. In S.N. Atluri, R. G.; Zienkiewicz, O. (eds): *Hybrid and Mixed Finite Element Methods*, pp. 51–71.

Babuska, I. (1973): The finite element method with Lagrangian multipliers. *Numerische Mathematik*, vol. 20, no. 3, pp. 179–192.

Bao, G.; Hutchinson, J. W.; McMeeking, R. M. (1991): Particle reinforcement of ductile matrices against plastic flow and creep. *Acta Metallurgica et Materialia*, vol. 39, no. 8, pp. 1871–1882.

Bratianu, C.; Atluri, S. N. (1983): A hybrid finite element method for stokes flow: part I -formulation and numerical studies. *Computer Methods in Applied Mechanics and Engineering*, vol. 36, pp. 23–37.

Brezzi, F. (1974): On the existence, uniqueness and approximation of saddle-point problems arising from Lagrangian multipliers. *Revue Française D'automatique, Informatique, Recherche Opérationnelle, Analyse Numérique*, vol. 8, no. 2, pp. 129–151.

Budiansky, B. (1965): On the elastic moduli of some heterogeneous materials. *J. Mech. Phys. Solids*, vol. 13, pp. 223–227.

Cai, Y. C.; Paik, J. K.; Atluri, S. N. (2009): Large deformation analyses of space-frame structures, with members of arbitrary cross-section, using explicit tangent stiffness matrices, based on a Von Karman type nonlinear theory in rotated reference frames. *CMES: Computer Modeling in Engineering & Sciences*, vol. 53, no. 2, pp. 117–145.

Cai, Y. C.; Paik, J. K.; Atluri, S. N. (2010): Locking-free thick-thin rod/beam element for large deformation analyses of space-frame structures, based on the Reissner variational principle and a Von Karman type nonlinear theory. *CMES: Computer Modeling in Engineering & Sciences*, vol. 58, no. 1, pp. 75–108.

Cai, Y. C.; Paik, J. K.; Atluri, S. N. (2010): A triangular plate element with drilling degrees of freedom, for large rotation analyses of built-up plate/shell structures, based on the reissner variational principle and the Von Karman nonlinear theory in the co-rotational reference frame. *CMES: Computer Modeling in Engineering & Sciences*, vol. 61, no. 3, pp. 273–312.

Cazzani, A.; Garusi, E.; Tralli, A.; Atluri, S. N. (2005): A four-node hybrid assumed strain finite element for laminated composite plates. *CMC: Computers, Materials & Continua*, vol. 2, no. 1, pp. 23–38.

Christman, T.; Needleman, A.; Suresh, S. (1989): An experimental and numerical study of deformation in metal-ceramic composites. *Acta Metallurgica*, vol. 37, no. 11, pp. 3029–3050.

Dong, L.; Atluri, S. N. (2011a): A simple procedure to develop efficient & stable

hybrid/mixed elements, and Voronoi cell finite elements for macro- & micromechanics. *CMC: Computers, Materials & Continua*, vol. 24, no. 1, pp. 61–104.

Dong, L.; Atluri, S. N. (2011b): Development of T-Trefftz four-node quadrilateral and Voronoi cell finite elements for macro- & micromechanical modeling of solids. *CMES: Computer Modeling in Engineering & Sciences*, vol. 81, no. 1, pp. 69–118.

Dong, L.; Atluri, S. N. (2012): T-Trefftz Voronoi cell finite elements with elastic/rigid inclusions or voids for micromechanical analysis of composite and porous materials. *CMES: Computer Modeling in Engineering & Sciences*, vol. 83, no. 2, pp. 183–220.

Eshelby, J. D. (1957): The determination of the elastic field of an ellipsoidal inclusion, and related problems. *Proc. R. Soc. Lond. A*, vol. 241, pp. 376–396.

Ghosh, S. (2011): *Micromechanical Analysis and Multi-Scale Modeling Using the Voronoi Cell Finite Element Method*. CRC Press/Taylor & Francis.

Ghosh, S.; Lee, K.; Moorthy, S. (1995): Multiple scale analysis of heterogeneous elastic structures using homogenization theory and Voronoi cell finite element method. *International Journal of Solids and Structures*, vol. 32, no. 1, pp. 27–62.

Ghosh, S.; Mallett, R. L. (1994): Voronoi cell finite elements. *Computers and Structures*, vol. 50, no. 1, pp. 33–46.

Ghosh, S.; Moorthy, S. (2004): Three dimensional Voronoi cell finite element model for microstructures with ellipsoidal heterogeneties. *Computational Mechanics*, vol. 34, pp. 510–531.

Ghosh, S.; Mukhopadhyay, S. N. (1991): A two-dimensional automatic mesh generator for finite element analysis for random composites. *Computers and Structures*, vol. 41, no. 2, pp. 245–256.

Golberg, M. A.; Chen, C. S.; Bowman, H. (1999): Some recent results and proposals for the use of radial basis functions in the BEM. *Engineering Analysis with Boundary Elements*, vol. 23, pp. 285–296.

Grujicic, M.; Zhang, Y. (1998): Determination of effective elastic properties of functionally graded materials using Voronoi cell finite element method. *Materials Science and Engineering A*251, pp. 64–76.

Hill, R. (1965): A self-consistent mechanics of composite materials. *J. Mech. Phys. Solids*, vol. 13, pp. 213–222.

Hori, M.; Nemat-Nasser, S. (1993): Double-inclusion model and overall moduli of multi-phase composites. *Mechanics of Materials*, vol. 14, pp. 189–206.

Lee, S.W.; Pian, T. H. H. (1978): Improvement of plate and shell finite elements by mixed formulations. *A. I. A. A. Journal*, vol. 16, no. 1, pp. 29–34.

Pian, T. H. H. (1964): Derivation of element stiffness matrices by assumed stress distribution. *A. I. A. A. Journal*, vol. vol.2, pp. 1333–1336.

Pian, T. H. H.; Mau, S. T. (1972): Some recent studies in assumed stress hybrid models. *Advances in Computational Methods in Structural Mechanics and Design*, Oden, Clought, Yamamoto (eds.), pp. 87-106.

Pian, T. H. H.; Sumihara, K. (1984): Rational approach for assumed stress finite elements. *International Journal for Numerical Methods in Engineering*, vol. 20, no. 9, pp. 1685–1695.

Pian, T. H. H.; Wu, C. (1983): A rational approach for choosing stress terms for hybrid finite element formulations. *International Journal for Numerical Methods in Engineering*, vol. 26, no. 10, pp. 2331–2343.

Punch, E. F.; Atluri, S. N. (1984): Applications of isoparametric three dimensional hybrid-stress finite elements with least-order stress fields. *Computers & Structures*, vol. 19, pp. 409–430.

Punch, E. F.; Atluri, S. N. (1984): Development and testing of stable, invariant, isoparametric curvilinear 2- and 3-D hybrid-stress elements. *Computer Methods in Applied Mechanics and Engineering*, vol. 47, no. 3, pp. 331–356.

Reissner, E. (1950): On a variational theorem in elasticity. *Journal of Mathematical Physics*, vol. 29, pp. 90–95.

Rubinstein, R.; Punch, E. F.; Atluri, S. N. (1984): An analysis of, and remedies for, kinematic modes in hybrid-stress finite elements: selection of stable, invariant stress fields. *Computer Methods in Applied Mechanics and Engineering*, vol. 38, no. 1, pp. 63–92.

Tang, L.; Chen, W.; Liu, Y. (1984): Formulation of quasi-conforming element and Hu-Washizu principle. *Computers & Structures*, vol. 19, no. 1-2, pp. 247–250.

Timoshenko, S. P.; Goodier, J. N. (1976): *Theory of Elasticity*. McGraw Hill, 3rd edition.

Tvergaard, V. (1990): Analysis of tensile properties for a whisker-reinforced metal-matrix composite. *Acta Metallurgica et Materialia*, vol. 38, no. 2, pp. 185– 194.

Wachspress, E. L. (1975): *A Rational Finite Element Basis*, *Mathematics in Science and Engineering*, vol. 114, Academic Press.

Wu, Z. (1995): Compactly supported positive definite radial functions. *Advances in Computational Mathematics*, vol. 4, no. 1, pp. 283–292.

Xue, W.; Karlovitz, L. A.; Atluri, S. N. (1985): On the existence and stability conditions for mixed-hybrid finite element solutions based on Reissner's variational principle. *International Journal of Solids and Structures*, vol. 21, no. 1, pp. 97–116.

Ying, L. A.; Atluri, S. N. (1983): A hybrid finite element method for stokes flow: Part II -stability and convergence studies. *Computer Methods in Applied Mechanics and Engineering*, vol. 36, pp. 39–60.

Zhai, P.; Jiang, C.; Zhang, Q. (1993): Ceramic Transactions: Functionally Gradient Materials, The American Ceramic Society, Westerville, OH, 1993, p. 449.

Zhu, H. H.; Cai, Y.; Paik, J. K.; Atluri, S. N. (2010): Locking-free thick-thin rod/beam element based on a Von Karman type nonlinear theory in rotated reference frames for large deformation analyses of space-frame structures. *CMES: Computer Modeling in Engineering & Sciences*, vol. 57, no. 2, pp. 175–20.